

Revisiting the Broken Symmetry Phase of Solid Hydrogen: A Neural Network Variational Monte Carlo Study

Shengdu Chai,^{1,2} Chen Lin,³ Xinyang Dong,⁴ Yuqiang Li,² Wanli Ouyang,^{2,5} Lei Wang,⁴ and X.C. Xie^{1,6,7}

¹*Interdisciplinary Center for Theoretical Physics and Information Sciences (ICTPIS), Fudan University, Shanghai 200433, China*

²*Shanghai Artificial Intelligence Laboratory, Shanghai 200232, China*

³*Department of Engineering, University of Oxford, Oxford OX1 4BH, UK*

⁴*Beijing National Laboratory for Condensed Matter Physics and Institute of Physics, Chinese Academy of Sciences, Beijing 100190, China*

⁵*Department of Information Engineering, The Chinese University of Hong Kong, Hong Kong SAR HKG, China*

⁶*International Center for Quantum Materials, School of Physics, Peking University, Beijing 100871, China*

⁷*Hefei National Laboratory, Hefei 230088, China*

(Dated: December 30, 2025)

The crystal structure of high-pressure solid hydrogen remains a fundamental open problem. Although the research frontier has mostly shifted toward ultra-high pressure phases above 400 GPa, we show that even the broken symmetry phase observed around 130 GPa requires revisiting due to its intricate coupling of electronic and nuclear degrees of freedom. Here, we develop a first principle quantum Monte Carlo framework based on a deep neural network wave function that treats both electrons and nuclei quantum mechanically within the constant pressure ensemble. Our calculations reveal an unreported ground-state structure candidate for the broken symmetry phase with *Cmcm* space group symmetry, and we test its stability up to 96 atoms. The predicted structure quantitatively matches the experimental equation of state and X-ray diffraction patterns. Furthermore, our group-theoretical analysis shows that the *Cmcm* structure is compatible with existing Raman and infrared spectroscopic data. Crucially, static density functional theory calculation reveals the *Cmcm* structure as a dynamically unstable saddle point on the Born-Oppenheimer potential energy surface, demonstrating that a full quantum many-body treatment of the problem is necessary. These results shed new light on the phase diagram of high-pressure hydrogen and call for further experimental verifications.

I. INTRODUCTION

Understanding the behavior of hydrogen under extreme pressure remains a grand challenge with profound implications [1–5], ranging from planetary interiors to the pursuit of the metallic, high-temperature superconducting state. Determining the precise structure is fundamental to these goals, as structure dictates the physical properties. Although decades of experimental effort have revealed a rich phase diagram, the detailed structures of high-pressure hydrogen remain largely unsettled. To date, only the structure of low-pressure Phase I is firmly confirmed by experiment as a hexagonal close-packed (hcp) lattice of freely rotating H₂ molecules [6–8]. With increasing pressure, the system transitions into a broken symmetry phase characterized by the emergence of long-range orientational order. While recent frontiers have advanced toward the ultra-high pressure regime (>400 GPa) in pursuit of metallic hydrogen, the detailed structures of the broken symmetry phase are less settled than commonly assumed and require revisiting.

Despite tremendous progress in experimental techniques [6–24], it is still difficult to unambiguously determine the structure of solid hydrogen under extreme conditions. The extreme pressure conditions and the small, fragile samples restrict feasible probes to low-power optical techniques such as Raman and infrared (IR) spectroscopy [9–19]. Moreover, the inherently weak X-ray

diffraction (XRD) signals of hydrogen [20–24] further hinder direct structural identification, making it difficult to discern the signatures of the high-pressure phases.

In light of these experimental difficulties, first principles calculations have proposed several candidate structures for broken symmetry phase, including *P2₁/c-8*, *P2₁/c-24*, *Pca₂1*, *Cmc2₁*, *P6₃/m*, etc. [25–41], and others even suggested that broken symmetry phase to be a “quantum fluxional solid” [42, 43]. However, these predictions have been inconclusive due to the inherent limitations of standard computational frameworks rooted in the Born-Oppenheimer (BO) approximation and the inadequate treatment of electronic correlations. Static Density Functional Theory (DFT) calculations [44–48] neglect the zero-point energy (ZPE) of protons, a contribution comparable to the cohesive energy in hydrogen, often leading to erroneous stability rankings. While *Ab initio* molecular dynamics (AIMD) [44, 49, 50] introduces thermal effects, it typically treats nuclei as classical particles, thereby missing critical nuclear quantum effects (NQEs) [51] such as tunneling and zero-point motion. Consequently, classical AIMD cannot intrinsically capture the distinct phase behaviors of isotopes. More advanced methods like path-integral molecular dynamics [44, 52] or path-integral quantum Monte Carlo [44, 53–55] rigorously incorporate NQEs and recover isotope effects; however, they rely on an underlying potential energy surface generated by DFT, thus inheriting the

systematic errors of approximate exchange-correlation functionals.

Crucially, the contribution of lattice anharmonicity, often neglected or treated insufficiently, is pivotal in determining the structural stability of solid hydrogen [56, 57]. Previous studies have shown that anharmonic correction is “small but significant” and impacts molecular and atomic phases oppositely, significantly shifting predicted phase boundaries [56]. Even state-of-the-art approaches designed to capture these effects, such as the stochastic self-consistent harmonic approximation (SSCHA) [57], remain constrained by the BO approximation and the assumption of a Gaussian nuclear density matrix. To accurately describe the phase diagram, it is therefore essential to transcend these limitations by employing a framework that supports an intrinsically non-Gaussian nuclear wavefunction, provides a highly accurate description of electronic correlations, and treats electrons and nuclei on an equal quantum footing to recover non-adiabatic effects.

Neural network based variational Monte Carlo calculation (NNVMC), pioneered by [58] and in particular Ref. [59] for *ab initio* simulations, has emerged as a powerful way to solve quantum many-body problems accurately and reliably [60, 61]. To date, there have been applications to a broad set of physical and chemical problems, including molecules [59, 62–66] and solid-state materials [67], moiré systems [68, 69], homogeneous electron gases [70–75], excitons [76], superfluids [77], high-pressure hydrogen [78–80], fractional quantum Hall states [81–84] and topological insulators [85]. Collectively, these studies establish neural-network quantum states as a versatile and systematically improvable framework for first-principle quantum many-body computation.

Building on this progress, we develop a beyond Born-Oppenheimer real-space neural network framework for enthalpy extremization to investigate solid hydrogen structures. By extending the NNVNC method to the constant pressure (NPT) ensemble [86], our framework simultaneously optimizes the crystal geometry and the full quantum many-body wave function for both electrons and nuclei [87]. Akin to the approach demonstrated in Refs. [80, 86], our framework employs a highly flexible, non-Gaussian representation of the nuclear wavefunction, thereby treating NQEs and electronic correlations on an equal footing without relying on the BO approximation under NPT ensemble.

In this paper, we apply this methodology to provide new insights into the long-standing issue of the broken symmetry phase of solid hydrogen. Our simulations identify a candidate orthorhombic ground-state structure with *Cmcm* space group symmetry. This structure exhibits good consistency with experimental observations, quantitatively reproducing key features of the latest XRD patterns. Furthermore, symmetry analysis shows that its vibrational modes align with the spectroscopic signatures observed in Raman and IR experiments, providing a candidate for the structure of the broken symmetry phase.

The remainder of the paper is organized as follows: Section II introduces the computational framework and the neural network ansatz; Section III presents the main results, including benchmark results and the newly identified *Cmcm* structure with its experimental signatures, and demonstrates through static DFT analysis the importance of a fully quantum many-body treatment of the problem; Section IV concludes with a discussion of the implications for the high-pressure hydrogen phase diagram and future directions. The code and discovered crystal structures are released at <https://github.com/DanChai22/BornFree>.

II. METHODS

We solve the ground state of the full Schrödinger equation for a system of N hydrogen atoms in a periodic simulation cell with constant pressure. The Hamiltonian is:

$$\hat{H} = -\frac{1}{2} \sum_{i=1}^N \nabla_{\mathbf{r}_i}^2 - \frac{1}{2M} \sum_{I=1}^N \nabla_{\mathbf{R}_I}^2 + V(\mathbf{r}, \mathbf{R}), \quad (1)$$

where $\mathbf{R} = \{\mathbf{R}_I\}$ and $\mathbf{r} = \{\mathbf{r}_i\}$ denote the proton and electron positions respectively. The first two terms denote the electron and proton kinetic energy respectively. The last term represents the Coulomb interaction, calculated with the Ewald summation technique. We adopt atomic units ($\hbar = e = m_e = 1$), consequently, energies are expressed in Hartree, lengths in Bohr, and the proton mass is set to $M = 1836$. The overall framework is illustrated in Fig. 1.

A. Wavefunction ansatz

Building a physically valid and expressive wave function is central to the success of the NNVNC framework. We parameterize the ground state wavefunction as a product of two components

$$\Psi(\mathbf{r}, \mathbf{R}) = \chi(\mathbf{R}) \varphi(\mathbf{r}, \mathbf{R}), \quad (2)$$

where we denote $\chi(\mathbf{R})$ as the nuclear wavefunction and $\varphi(\mathbf{r}, \mathbf{R})$ as the electronic wavefunction. Note that Eq. (2) is different from the Born-Huang expansion [88] in which $\varphi(\mathbf{r}, \mathbf{R})$ is treated as electronic eigenstates given nuclear positions. On the other hand, we do not deem $\varphi(\mathbf{r}, \mathbf{R})$ to be normalized with respect to the electron coordinates either. Hence, such an ansatz is not the same as the exact factorization ansatz [89, 90]. Eq. (2) is just a convenient factorization for the ground state wavefunction of the electron-nuclei coupled system in Eq. (1), designed to capture the coupled electron-nuclear quantum dynamics without the BO approximation.

We discuss the symmetry requirement of the wavefunctions and their neural network parameterizations in

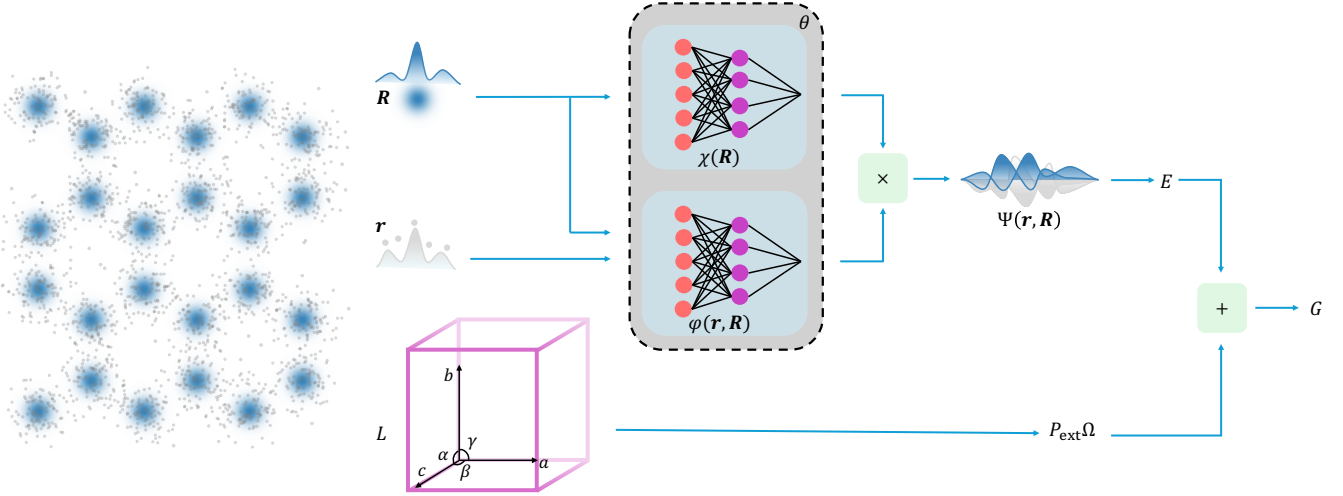


FIG. 1. **The computational framework.** The nuclear coordinates \mathbf{R} and the electron coordinates \mathbf{r} are fed into two neural networks that generate the nuclear wave function $\chi(\mathbf{R})$ and the electronic wave function $\varphi(\mathbf{r}, \mathbf{R})$, respectively. Their product, $\Psi(\mathbf{r}, \mathbf{R}) = \chi(\mathbf{R}) \varphi(\mathbf{r}, \mathbf{R})$, defines the total trial wave function. Together with the lattice parameters, they determine the enthalpy of the system $G = E + P_{\text{ext}}\Omega$, where P_{ext} is the external pressure and Ω the cell volume. Treating the enthalpy as the objective function, the lattice parameters L are optimized via simulated annealing, whereas the neural-network parameters θ are optimized by gradient descent.

the following. $\varphi(\mathbf{r}, \mathbf{R})$ must be antisymmetric under exchange of electrons and obey periodic boundary conditions (PBCs). $\chi(\mathbf{R})$ must obey PBCs as well, while nuclear exchange symmetry is neglected, since its energy scale is negligible compared to the nuclear kinetic energy [91]. We also note that while nuclear spin statistics (para- vs. ortho-hydrogen) are energetically crucial for the rotationally disordered Phase I [92, 93], they become secondary in the broken symmetry phases focused on here, where hindered molecular rotations diminish the impact of specific spin configurations. Thus the spin statistics are also neglected.

To rigorously enforce translational invariance under PBCs, all network inputs are constructed from periodic descriptors. We encode particle relative positions using sine and cosine of fractional coordinates [70], and construct single- and two-particle features $\mathbf{h}_{\alpha\beta}^1$, where α, β denote any pair of particles (electron-electron, nucleus-nucleus, or electron-nucleus). The superscript denotes that it is the input feature of the first layer of the neural network.

The explicit, flexible parameterization of the nuclear wavefunction $\chi(\mathbf{R})$ is a central feature of our ansatz. The nuclear log-amplitude $\ln \chi(\mathbf{R})$ is constructed from ion-ion features $\mathbf{h}_{i,j}^1$ processed by a deep residual network. We employ a ReZero scheme [94], which introduces a trainable scaling parameter initialized to zero. This design allows the model to start from a physically meaningful periodic distance metric and progressively learn many-body corrections d_{IJ}^{env} , thereby capturing anharmonicity in the nuclear wave function. The final log-probability is a sum of squared deviations from learned

equilibrium distances b_{IJ} with weight σ_{IJ} as follows:

$$\ln \chi(\mathbf{R}) = - \sum_{IJ} \sigma_{IJ}^2 (d_{IJ}^{\text{env}} - b_{IJ})^2 \quad (3)$$

The electronic wave function is developed based on DeepSolid [67], where antisymmetry is enforced through the product of spin-resolved Slater determinants,

$$\varphi(\mathbf{r}, \mathbf{R}) = \det[\phi_i^\uparrow] \det[\phi_i^\downarrow], \quad (4)$$

Single-particle orbitals $\phi_i^\alpha(\mathbf{r}_j; \mathbf{r}_{\neq j})$ are constructed from residual networks acting on electron-ion features $\mathbf{h}_{i,I}^1$ and electron-electron features $\mathbf{h}_{i,j}^1$, mixing single- and two-body embeddings across layers to encode higher-order correlations.

Although our implementation follows the overall architecture of DeepSolid, we introduce two key modifications to the original framework to enhance training stability. First, we utilize the sine and cosine periodic embedding [70], discussed previously, replacing the Jastrow factor-based embedding proposed in Ref. [95] to ensure smoother feature representation. Second, we simplify the electron features construction process. While the original DeepSolid constructs single-electron features based on the primitive cell, we found this approach led to training instability in hydrogen systems. We therefore bypass the primitive cell construction entirely and operate directly within the simulation cell.

B. Constant-Pressure Optimization

In the NPT ensemble, the loss function is the enthalpy:

$$G = \langle \Psi | \hat{G} | \Psi \rangle = \int d\mathbf{r} d\mathbf{R} |\Psi(\mathbf{r}, \mathbf{R})|^2 G_{\text{loc}}(\mathbf{r}, \mathbf{R}), \quad (5)$$

where $\hat{G} = \hat{H} + P_{\text{ext}}\Omega$, P_{ext} is the external pressure, and Ω is the cell volume; $G_{\text{loc}}(\mathbf{r}, \mathbf{R}) = \Psi^{-1}(\mathbf{r}, \mathbf{R})\hat{G}\Psi(\mathbf{r}, \mathbf{R})$ is the local enthalpy. As shown in Ref. [86], the structure of the wave function allows the enthalpy gradient,

$$\nabla_{\Theta} G = 2\mathbb{E}[(G_{\text{loc}} - \mathbb{E}[G_{\text{loc}}]) \nabla_{\Theta} \ln |\Psi_{\Theta}|] + \mathbb{E}[\nabla_{\Theta} G_{\text{loc}}], \quad (6)$$

to be decomposed into two distinct contributions. Here Θ collectively denotes the neural network parameters θ and the lattice parameters L . When optimizing θ at fixed L , only the first term contributes; conversely, when optimizing L at fixed θ , only the second term contributes.

However, direct evaluation of the second term, $\mathbb{E}[\nabla_{\Theta} G_{\text{loc}}]$, is computationally expensive. In practice, we avoid computing this costly term explicitly and instead optimize L via a stochastic simulated annealing procedure, as described below.

At each step, a trial lattice deformation $L \rightarrow L'$ is proposed, and the corresponding enthalpy G' is then evaluated. The move is accepted with the Metropolis acceptance probability $\min(1, e^{-\Delta G/\tau})$, where $\Delta G = G' - G$ and τ is the fictitious temperature, which is used to avoid the risk of trapping in shallow local minima. The fictitious temperature is decreased according to the Lundy–Mees schedule [96], $\tau(t) = \frac{\tau_0}{1+\beta t}$, ensuring ergodicity at early stages and convergence toward low-enthalpy configurations as the annealing progresses. Here, τ_0 is the initial temperature and β is the cooling rate.

A subtle point is that the enthalpies G and G' computed in VMC contain intrinsic statistical noise. Using these noisy estimates directly in the Metropolis violates detailed balance. Although the penalty methods can be used to restore exact Boltzmann distribution in the presence of noise [97], our goal is not to generate an NPT equilibrium distribution but to locate the minimum-enthalpy structure without evaluating high-order derivatives. In this optimization context, strict detailed balance is unnecessary, and the noise can even be beneficial [98].

C. Sampling

To evaluate the loss function and its gradient with respect to the neural network parameters θ , we sample electron and nuclear configurations from $p(\mathbf{r}, \mathbf{R}) = |\Psi(\mathbf{r}, \mathbf{R})|^2$. A naive one-shot Metropolis update in the joint electron–nuclear space is inefficient and often exhibits low acceptance rates for nuclear moves due to the vast disparity in energy scales between electrons and nuclei. We therefore employ a *Gibbs block sampler*: in each sweep, we (i) sample electronic coordinates \mathbf{r} from $p(\mathbf{r}|\mathbf{R})$

with fixed nuclei, followed by (ii) sample nuclear coordinates \mathbf{R} from $p(\mathbf{R}|\mathbf{r})$ with fixed electrons. Each conditional update uses Metropolis–Hastings algorithm, with adaptive step sizes to maintain target acceptance.

III. RESULTS

We first present benchmark calculations of hydrogen with dynamic protons and then move on to the discovered *Cmcm* structure for the broken symmetry phase of hydrogen. We will analyze its experimental signatures as well as its stability in more conventional DFT calculations with the BO approximation. These analyses place our computational discovery in context and highlight the importance of a fully quantum treatment of both electrons and nuclei.

A. Benchmarks

VMC/DMC has long been a cornerstone method for investigating the phase diagram of dense hydrogen [37, 91, 99–105]. Given the extensive body of literature available for validation, we first benchmark our method against established VMC/DMC results. Calculations were performed for systems of 54 hydrogen atoms arranged in a BCC lattice with fixed volume at $r_s = 1.31$.

Reference data for Slater–Jastrow wave functions using LDA–DFT orbitals (SJ–LDA) and backflow plane-wave orbitals (BF–PW) were taken from Ref. [105], while neural quantum state (NQS) energies were obtained from Ref. [80]. A detailed comparison is presented in Table I.

Our energies are consistently lower than those of all reference methods, including both traditional and neural quantum state approaches, while maintaining comparable energy variances. This indicates that our ansatz offers enhanced expressivity for the solid hydrogen ground state.

TABLE I. Ground-state energies for $N = 54$ hydrogen atoms arranged into a BCC lattice with $r_s = 1.31$ treated in full quantum manner. The digits in the brackets represent the statistical uncertainty of the energy and corresponding variance.

Variational ansatz	E/N	σ^2/N
SJ–LDA (VMC) [105]	-0.5195(2)	-
SJ–LDA (DMC) [105]	-0.52415(5)	-
BF–PW (VMC) [105]	-0.52194(5)	0.025(1)
BF–PW (DMC) [105]	-0.52610(7)	-
NQS (VMC) [80]	-0.52854(9)	0.0088(1)
Present Work	-0.529674(5)	0.01575(5)

B. The discovered *Cmcm* structure

Having validated our framework, we applied it to determine the structure of solid hydrogen at 130 GPa—corresponding to the experimental pressure range of broken symmetry phase. NPT simulations were performed on a system comprising 64 protons and 64 electrons. We began by optimizing the most promising candidate, $P2_1/c$ [41], whose optimization was initiated at an external pressure of $P_{\text{ext}} = 10$ GPa, and then gradually increased the pressure to 130 GPa. We found that the structure converged to an orthorhombic structure with *Cmcm* space-group symmetry, both at $P_{\text{ext}} = 95$ GPa and $P_{\text{ext}} = 130$ GPa.

To assess the robustness of this result, we performed independent optimizations starting from several structurally distinct configurations, including $Pca2_1$, $P6_3/m$, and $P6_3/mmc$ (with aligned molecules), as well as the identified *Cmcm* structure. This extensive search yielded two consistent outcomes. First, relaxations starting from both *Cmcm* and $Pca2_1$ converged to the lowest enthalpies, which were significantly lower—by at least 4 mHa per atom—than those of the $P6_3/mmc$ and $P6_3/m$ phases at 130 GPa. Second, the optimization initialized from $Pca2_1$ not only matched the final enthalpy of the *Cmcm* structure but also evolved into the *Cmcm* symmetry, differing only slightly in lattice aspect ratios. Similarly, calculations initialized directly in *Cmcm* remained stable. Finally, a separate optimization with 96 atoms starting from the *Cmcm* structure was carried to examine the stability of this structure with respect to system size, and the *Cmcm* lattice remains stable upon scaling. The convergence from multiple unrelated initial configurations suggests that the orthorhombic *Cmcm* lattice appears to be the enthalpy minimum within our calculation framework. To extract the equilibrium structure from the optimized configurations, we align the first atom in each batch after training.

Structurally, the discovered orthorhombic *Cmcm* phase contains 8 H_2 molecules per primitive unit cell (16 molecules in the conventional cell), as illustrated in Fig. 2. To obtain the structure, we align the first atom in each batch after training. The 32 hydrogen atoms fully occupy the four $8g$ Wyckoff positions. Notably, this proposed structure can be viewed as a distortion of the hcp structure found in Phase I, consistent with the indirect reconstructive mechanism discussed in previous works [22, 106]. Furthermore, the predicted structural parameters show good agreement with experimental measurements. At 130 GPa, our calculated equilibrium volume is $2.063 \text{ \AA}^3/\text{atom}$, within 4.3% of the experimental value ($2.156 \text{ \AA}^3/\text{atom}$) reported by Ji *et al.* [20]. This geometric consistency supports the reliability of the identified phase.

Beyond the lattice symmetry, a defining feature of the identified *Cmcm* structure is the orientational order of H_2 molecules. Unlike in Phase I, where the molecules undergo nearly free rotation, the broken symmetry phase

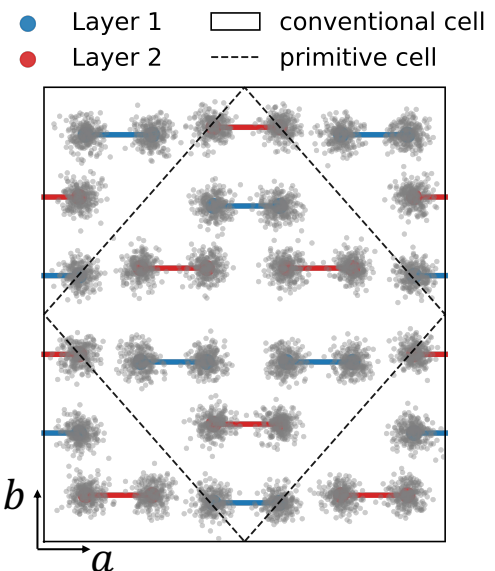


FIG. 2. The structure with lowest enthalpy discovered at 130 GPa for the broken symmetry phase solid hydrogen. The figure shows the projection of H_2 molecules onto the ab plane. Blue and red lines represent hydrogen molecules in the first and second layers along c axis, respectively. The black dashed line outlines the primitive cell, while the black solid line indicates the conventional cell. 32 hydrogen atoms in the conventional cell fully occupy four $8g$ Wyckoff positions of the space group *Cmcm*.

exhibits distinct orientational ordering that breaks the high symmetry of the hcp lattice. To quantify this ordering, we computed the joint angular distribution $g(\theta, \phi)$ by accumulating statistics across the sampled configurations. For each molecule, the orientation is characterized by the polar angle θ and the azimuthal angle ϕ as shown in Fig. 3. The resulting histogram was normalized to yield the probability density. As shown in Fig. 3, the molecules adopt a layered configuration, lying approximately within the ab plane. This orientational order naturally explains why the observed $c/a = 1.586$ in experiment [20] is slightly smaller than the ideal close-packed value of 1.63. Further analysis shows that rotational motion is largely suppressed, while librations persist within the ac plane, confined to an angular range of approximately $60^\circ < \theta < 120^\circ$.

A notable feature emerging from the converged *Cmcm* structure is the substantial contribution of the beyond BO term to the nuclear kinetic energy. We define the nuclear kinetic energy under the BO approximation (K_{BO}) and the beyond BO correction ($K_{\text{non-BO}}$) as $K_{\text{BO}} = -\frac{1}{2M} \sum_{I=1}^N \left\langle \frac{\nabla_{\mathbf{R}_I}^2 \chi(\mathbf{R})}{\chi(\mathbf{R})} \right\rangle$, and $K_{\text{non-BO}} = -\frac{1}{2M} \sum_{I=1}^N \left\langle \frac{\nabla_{\mathbf{R}_I}^2 \varphi(\mathbf{r}, \mathbf{R})}{\varphi(\mathbf{r}, \mathbf{R})} + 2\nabla_{\mathbf{R}_I} \varphi(\mathbf{r}, \mathbf{R}) \cdot \nabla_{\mathbf{R}_I} \chi(\mathbf{R}) \right\rangle$, where the expectation is for the samples from the joint wavefunction. In the relaxed *Cmcm* configuration, we

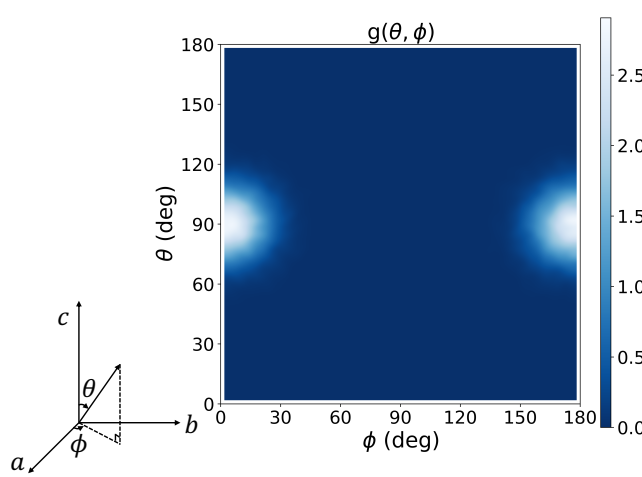


FIG. 3. Orientation order of the structure shown in Fig. 2. The angular distribution $g(\theta, \phi)$ illustrates that preferred orientations of H_2 molecules are within the ab plane. The color bar denotes the normalized density.

found that the $K_{\text{non-BO}}$ (~ 1.5 mHa per atom) accounts for approximately 30% of the K_{BO} . This significant contribution highlights the essential role of nuclear quantum effects in stabilizing the orthorhombic structure and suggests that the emergence of this specific structure is intrinsically driven by the beyond BO treatment within our framework.

C. Experimental signatures

1. X-ray diffraction

Direct comparison between simulated and experimental XRD patterns supports the $Cmcm$ structure. As shown in Fig. 4, the simulated XRD pattern based on the $Cmcm$ structure reproduces the experimental data of Ji *et al.* [20] with good fidelity. Although the third peak is relatively weak, its intensity can be enhanced by fine-tuning the atomic positions within the constraints of the same Wyckoff sites. Notably, simulated patterns for other proposed candidate structures, such as $P2_1/c$ -8, $P2_1/c$ -24, $Pca2_1$, and $P6_3/m$, exhibit subtle discrepancies compared to the experimental results. In all cases, the volume is scaled to the experimental volume at the same pressure. The agreement between experiment and simulation therefore provides a structural fingerprint, supporting the assignment of Phase II hydrogen as a $Cmcm$ structure.

2. Vibrational spectroscopy

Vibrational spectroscopy offers an independent probe of structural symmetry. Experimentally, the transition

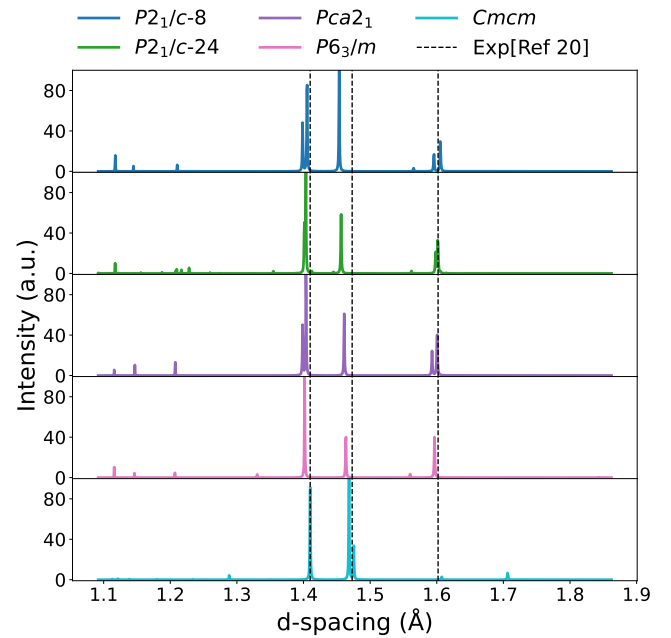


FIG. 4. The simulated XRD pattern for various candidate structures at 130 GPa compared with the experimental observation [20].

from Phase I to Phase II is marked by the appearance of new, broadened vibron features in both Raman and IR spectra, absent in the high-symmetry Phase I, indicating a lowering of lattice symmetry.

We performed a group-theoretical analysis of the vibrational modes for the $Cmcm$ structure to evaluate its spectroscopic characteristics as reference. As summarized in Table II, this symmetry admits four IR-active and four Raman-active vibrons. Although the theoretical mode count exceeds current experimental observations, the $Cmcm$ symmetry remains compatible with the data, as the experimentally observed features can be interpreted as a subset of the theoretically allowed active modes.

The analysis of the lattice phonon modes presents a greater challenge due to limited experimental data in the low-frequency region. As shown in Table II, the $Cmcm$ structure allows for a rich spectrum of phonon modes. However, no IR phonon modes have been reported in the literature to our knowledge. Similarly, the Raman phonon features are elusive; while earlier work reported a single peak [19], subsequent studies observed that this phonon mode becomes extremely weak [15]. The absence of these theoretical peaks in current data is likely attributable to weak signal intensities [32] or peak overlapping characteristic of high-pressure hydrogen experiments, rather than an exclusion of the $Cmcm$ symmetry.

TABLE II. Summary of theoretical predictions and experimental observations on IR and Raman modes. Question marks (?) denote that the corresponding phonon modes are currently unreported or unresolvable. To our knowledge, the IR phonon is not reported in the literature, and the Raman phonon is reported as a single peak in [19], while Hemley *et al.* [15] observed that this phonon mode becomes extremely weak.

Space group	IR vibron	Raman vibron	IR phonon	Raman phonon
$Pca2_1$ [107]	$A_1 + B_1 + B_2$	$A_1 + A_2 + B_1 + B_2$	$2A_1 + 2B_1 + 2B_2$	$2A_1 + 3A_2 + 2B_1 + 2B_2$
$P2_1/c$ [107]	$A_u + B_u$	$A_g + B_g$	$2A_u + B_u$	$3A_g + 3B_g$
$P6_3/m$ [107]	E_{1u}	$2A_g + E_{2g}$	$A_u + 2E_{1u}$	$2A_g + E_{1g} + 3E_{2g}$
$Cmcm$	$3B_{2u} + B_{3u}$	$3A_g + B_{1g}$	$3B_{2u} + 6B_{1u} + 3B_{3u}$	$4B_{1g} + 7B_{3g} + 4A_g + 5B_{2g}$
Experiments [15, 19, 108]	2	1	?	?

D. Stability analysis with static DFT calculations

To understand why the $Cmcm$ structure identified in our calculation was not found in previous DFT-based searches, we performed static DFT calculations using the PBE functional. We conducted variable-cell relaxations (`vc-relax`) on the $Cmcm$ structure alongside other competitive candidates ($P2_1/c-8$, $Pca2_1$, $P6_3/m$ with unit cells containing 64 atoms, and $P2_1/c-24$ with 48 atoms). Convergence was strictly verified with Monkhorst-Pack \mathbf{k} -point meshes up to $8 \times 8 \times 8$, ensuring that finite-size errors do not affect our conclusions.

Our static DFT results reveal a significant discrepancy with the NNVNC ground state. Across all tested structures, the relaxed space groups remained unchanged during the `vc-relax`. Apart from $Cmcm$, all other candidates exhibit very similar final enthalpies per atom at a given \mathbf{k} -point mesh. In contrast to our calculation, the static enthalpy of $Cmcm$ is not the global minimum, it lies approximately 1.1 mHa/atom higher than $Pca2_1$. To further assess the dynamical stability, we computed the phonon spectrum. While other candidates are dynamically stable, the relaxed $Cmcm$ structure exhibits negative (imaginary) frequencies at the Γ point. This shows that on the classical BO surface, the $Cmcm$ lattice is a saddle point rather than a stable minimum.

The fact that $Cmcm$ is a saddle point with higher static enthalpy explains its absence in conventional DFT searches. There are several possibilities for such discrepancy as the static DFT calculation involves multiple approximations that we have relaxed in our many-body calculation. First, there are DFT functional errors [36]. Second, it is well known that strong NQEs, including ZPE, lattice anharmonicity, and even beyond BO effects, may overturn classical structural predictions. A detailed assessment is beyond the scope of the present paper. In the following, we speculate on the effects of lattice anharmonicities and beyond BO contributions in stabilizing the discovered $Cmcm$ phase.

First, NQEs such as ZPE and anharmonicity play a critical role. Although the static enthalpy of $Cmcm$ is higher than that of $Pca2_1$, the difference is small (~ 1.1 mHa/atom). Once NQEs are considered,

the energetic ordering can be reversed. The ZPE of solid hydrogen at this pressure is estimated to be around 10 mHa/atom based on harmonic phonon calculations [109]. Therefore, even a moderate estimate that different competing structures differ by 10% in their ZPE is comparable to the ~ 1 mHa/atom difference between the static-lattice enthalpy of $Cmcm$ and $Pca2_1$ structures.

Second, our framework explicitly captures non-BO effects. As detailed in Sec. III B, the non-BO contribution to the kinetic energy in the $Cmcm$ phase is substantial (~ 1.5 mHa/atom). This correction alone significantly influences the PES. Since standard DFT is confined to the BO approximation, it inherently misses this stabilizing energy contribution.

Taken together, these results demonstrate that $Cmcm$ is not stable at the static-lattice level within the PBE functional. Instead, its emergence as the enthalpy-minimizing structure in our framework is driven by strong NQEs, including anharmonicity and non-BO effects. This physical picture is consistent with a large body of recent work on hydrogen-rich systems. Errea *et al.* [110] shows that quantum fluctuations reshape the BO landscape of LaH_{10} , collapsing multiple classical minima into a single high-symmetry phase; and Monserrat *et al.* [111] demonstrates how anharmonic and quantum effects stabilize otherwise classically-unstable high-pressure hydrogen phases. Similarly, our findings also suggest that strong protonic quantum motion may effectively lift the saddle point on the BO surface, transforming it into a minimum on the full quantum energy landscape.

These observations not only explain why previous DFT-based searches missed the $Cmcm$ structure but also highlight the importance of a fully anharmonic and beyond BO description, such as that provided by our method, for correctly determining the phase diagram of dense solid hydrogen.

IV. DISCUSSION AND CONCLUSION

The present work revisits one of the longest-standing problems in high-pressure physics—the structural nature of the broken symmetry phase of solid hydrogen. By employing NNVNC framework, which treats electrons and nuclei on an equal footing and directly minimizes enthalpy in the NPT ensemble, we identify an orthorhombic molecular lattice with *Cmcm* symmetry as the robust ground-state structure at 130 GPa. This identification is supported by three independent benchmarks: (1) agreement with the experimental equation of state, (2) match with the experimental XRD pattern, and (3) consistency with the complex Raman and infrared spectroscopic signatures that define the transition into broken symmetry phase. Taken together, these results shed new light on the structural nature of the broken symmetry phase hydrogen and may provide insight into understanding the subsequent evolution toward metallic hydrogen.

An intriguing question is whether the structural transition of the H_2 hcp structure coincides with the orientational ordering H_2 molecules. Our analysis suggests that these may be two distinct symmetry breaking transitions. As noted in Ref. [106], the *Cmcm* symmetry is a maximal subgroup of the Phase I *P6₃/mmc* space group. In the model proposed by Toledano *et al.*, H atoms in Phase I partially occupy the $4f$ and $12k$ sites, reflecting the orientational disorder of freely rotating molecules. They proposed that compression induces a transition to a partially ordered *Cmcm* phase, where fractional occupancy persists (e.g., half-filled $8f$ and $16h$ sites), leading to orientational degeneracy and potential topological frustration that could drive an incommensurate modulation.

In contrast, our calculations suggest that the broken symmetry phase is fully ordered, characterized by full occupancy of the $8g$ Wyckoff positions of the *Cmcm* space group. The subgroup pathway inferred from our calculations differs from that of Ref. [106]. To link our *Cmcm* structure to Phase I, we consider a restricted *P6₃/mmc* model where molecules are confined to the *ab* plane (corresponding to partially occupied $6h$ sites, derived from $12k$ with $z = 1/4$ and the $4f$ sites are vacated). Under the group–subgroup reduction $P6_3/mmc \rightarrow Cmcm$, these partially occupied $6h$ sites split into the fully occupied $8g$ positions of the *Cmcm* structure. Consequently, the resulting phase is free of orientational degeneracy, eliminating the mechanism previously hypothesized to drive incommensurate distortion. Furthermore, unlike many previously proposed candidate structures where molecular centers of mass (COM) retain the hcp lattice positions of Phase I, the COMs in our discovered *Cmcm* structure exhibit a more complex structure. While the COMs no longer form a simple hcp lattice, the structure can be fundamentally viewed as a distortion of hcp. This symmetry analysis hints at a possible two-step transformation sequence involving an intermediate state that retains *P6₃/mmc* lattice symmetry but lacks free rotation. Further investigation into the coupling between lattice

symmetry breaking and orientational ordering is warranted.

On the methodological front, similar to the beyond BO neural wavefunction approach in Ref. [80], we have developed a general first principle framework for predicting ground states of quantum materials beyond BO approximation within NPT ensemble. The necessity of such an approach is underscored by our stability analysis in Sec. III D, which reveals that the *Cmcm* structure is a saddle point on the static PES. It is stabilized only by strong nuclear quantum effects—specifically, the interplay of zero-point motion and non-adiabatic coupling. By treating variable cell parameters as variational degrees of freedom and minimizing the enthalpy of a coupled electron-nuclear wavefunction, our calculations capture these critical stabilizing mechanisms that standard DFT methods inherently miss. Consequently, the optimal crystal structure emerges naturally as an intrinsic property of the many-body quantum ground state. Scalable to systems with hundreds of quantum particles, this approach provides a versatile tool for investigating systems where quantum fluctuations reshape the energy landscape, making it particularly well suited for exploring higher-pressure hydrogen phases, high- T_c hydrides, and other light-element materials under extreme conditions.

In conclusion, our calculations with full quantum-many accuracy identify the broken symmetry phase as an orthorhombic *Cmcm* molecular crystal. This finding sheds new light to a long-standing problem in high-pressure physics, reconciling theory with experiment across structural, spectroscopic, and thermodynamic observations. Beyond establishing the structure of this phase, the present work explores a general computational framework for predicting quantum materials under finite pressure, treating electronic and nuclear degrees of freedom on an equal footing. Crucially, our results show that a full non-adiabatic quantum treatment, capturing anharmonicity and beyond BO effects, plays an important role in describing the phase diagram of dense hydrogen. The identification of the *Cmcm* structure not only clarifies the nature of the broken symmetry phase but also marks a leap toward understanding hydrogen’s phase diagram.

ACKNOWLEDGMENTS

We thank David Ceperley, Hao Xie, Mao Su, Gengyuan Hu, Zi-Xiao Zhang, Cheng Chen, Hongfang Liu for helpful discussions. This work is supported by the National Natural Science Foundation of China under Grants No. T2225018, No. 92270107, No. 12188101, No. T2121001, No. 12504289, the Strategic Priority Research Program of the Chinese Academy of Sciences under Grants No. XDB0500000, and the National Key Projects for Research and Development of China Grants No. 2021YFA1400400, Quantum Science and Technology-National Science and Technology Major

Project (Grants No. 2021ZD0302400).

[1] T. Guillot, The interiors of giant planets: Models and outstanding questions, *Annual Review of Earth and Planetary Sciences* **33**, 493–530 (2005).

[2] J. M. McMahon, M. A. Morales, C. Pierleoni, and D. M. Ceperley, The properties of hydrogen and helium under extreme conditions, *Reviews of Modern Physics* **84**, 1607 (2012).

[3] E. Gregoryanz, C. Ji, P. Dalladay-Simpson, B. Li, R. T. Howie, and H.-K. Mao, Everything you always wanted to know about metallic hydrogen but were afraid to ask, *Matter and Radiation at Extremes* **5**, 38101 (2020).

[4] E. Wigner and H. B. Huntington, On the Possibility of a Metallic Modification of Hydrogen, *The Journal of Chemical Physics* **3**, 764 (1935).

[5] N. W. Ashcroft, Metallic hydrogen: A high-temperature superconductor?, *Phys. Rev. Lett.* **21**, 1748 (1968).

[6] R. M. Hazen, H. K. Mao, L. W. Finger, and R. J. Hemley, Single-crystal x-ray diffraction of n - H 2 at high pressure, *Physical Review B* **36**, 3944 (1987).

[7] H. K. Mao, A. P. Jephcoat, R. J. Hemley, L. W. Finger, C. S. Zha, R. M. Hazen, and D. E. Cox, Synchrotron X-ray diffraction measurements of single-crystal hydrogen to 26.5 gigapascals, *Science* **239**, 1131 (1988).

[8] R. J. Hemley, H. K. Mao, L. W. Finger, A. P. Jephcoat, R. M. Hazen, and C. S. Zha, Equation of state of solid hydrogen and deuterium from single-crystal x-ray diffraction to 26.5 GPa, *Physical Review B* **42**, 6458 (1990).

[9] P. Loubeyre, F. Occelli, and P. Dumas, Compression of D2 to 460 GPa and isotopic effects in the path to metal hydrogen, *Physical Review Letters* **129**, 35501 (2022).

[10] Y. Akahama, Y. Mizuki, S. Nakano, N. Hirao, and Y. Ohishi, Raman scattering and X-ray diffraction studies on phase III of solid hydrogen, *Journal of Physics: Conference Series* **950**, 42060 (2017).

[11] A. F. Goncharov, R. J. Hemley, H.-k. Mao, and J. Shu, New high-pressure excitations in parahydrogen, *Physical Review Letters* **80**, 101 (1998).

[12] A. F. Goncharov, R. J. Hemley, and H.-k. Mao, Vibron frequencies of solid H2 and D2 to 200 GPa and implications for the $P - T$ phase diagram, *Journal of Chemical Physics* **134**, 174501 (2011).

[13] A. F. Goncharov, E. Gregoryanz, R. J. Hemley, and H.-k. Mao, Spectroscopic studies of the vibrational and electronic properties of solid hydrogen to 285 GPa, *Proceedings of the National Academy of Sciences* **98**, 14234 (2001).

[14] R. J. Hemley and H. K. Mao, Phase transition in solid molecular hydrogen at ultrahigh pressures, *Physical Review Letters* **61**, 857 (1988).

[15] R. J. Hemley, A. F. Goncharov, H.-k. Mao, E. Karmon, and J. H. Eggert, Spectroscopic studies of p-H2 to above 200 GPa, *Journal of Low Temperature Physics* **110**, 75 (1998).

[16] X.-D. Liu, High-pressure behavior of hydrogen and deuterium at low temperatures, *Physical Review Letters* **119**, 10.1103/PhysRevLett.119.065301 (2017).

[17] H. E. Lorenzana, I. F. Silvera, and K. A. Goettel, Orientational phase transitions in hydrogen at megabar pressures, *Physical Review Letters* **64**, 1939 (1990).

[18] I. I. Mazin, R. J. Hemley, A. F. Goncharov, M. Hanfland, and H.-k. Mao, Quantum and classical orientational ordering in solid hydrogen, *Physical Review Letters* **78**, 1066 (1997).

[19] R. J. Hemley, H. K. Mao, and J. F. Shu, Low-frequency vibrational dynamics and structure of hydrogen at megabar pressures, *Physical Review Letters* **65**, 2670 (1990).

[20] C. Ji, B. Li, W. Liu, J. S. Smith, A. Majumdar, W. Luo, R. Ahuja, J. Shu, J. Wang, S. Sinogeikin, Y. Meng, V. B. Prakapenka, E. Greenberg, R. Xu, X. Huang, W. Yang, G. Shen, W. L. Mao, and H.-K. Mao, Ultrahigh-pressure isostructural electronic transitions in hydrogen, *Nature* **573**, 558 (2019).

[21] C. Ji, B. Li, J. Luo, Y. Zhao, Y. Liu, K. Glazyrin, A. Björling, L. A. B. Marçal, M. Kahnt, S. Kalbfleisch, W. Liu, Y. Gao, J. Wang, W. L. Mao, H. Liu, Y. Ma, Y. Ding, W. Yang, and H.-K. Mao, Ultrahigh-pressure crystallographic passage towards metallic hydrogen, *Nature* **641**, 904 (2025).

[22] Y. Akahama, M. Nishimura, H. Kawamura, N. Hirao, Y. Ohishi, and K. Takemura, Evidence from x-ray diffraction of orientational ordering in phase III of solid hydrogen at pressures up to 183 GPa, *Physical Review B* **82**, 60101 (2010).

[23] I. Goncharenko and P. Loubeyre, Neutron and X-ray diffraction study of the broken symmetry phase transition in solid deuterium, *Nature* **435**, 1206 (2005).

[24] P. Loubeyre, R. LeToullec, D. Hausermann, M. Hanfland, R. J. Hemley, H. K. Mao, and L. W. Finger, X-ray diffraction and equation of state of hydrogen at megabar pressures, *Nature* **383**, 702 (1996).

[25] J. Kohanoff, Solid molecular hydrogen: The broken symmetry phase, *Physical Review Letters* **78**, 2783 (1997).

[26] K. Nagao, *Ab Initio* calculation of optical-mode frequencies in compressed solid hydrogen, *Physical Review B* **59**, 13741 (1999).

[27] H. Kitamura, S. Tsuneyuki, T. Ogitsu, and T. Miyake, Quantum distribution of protons in solid molecular hydrogen at megabar pressures, *Nature* **404**, 259 (2000).

[28] M. Städele and R. M. Martin, Metallization of molecular hydrogen: Predictions from exact-exchange calculations, *Physical Review Letters* **84**, 6070 (2000).

[29] K. A. Johnson and N. W. Ashcroft, Structure and bandgap closure in dense hydrogen, *Nature* **403**, 632 (2000).

[30] L. J. Zhang, Y. L. Niu, T. Cui, Y. Li, Y. Wang, Y. M. Ma, Z. He, and G. T. Zou, Ab initio lattice dynamics evidence for the broken-symmetry phase of solid hydrogen, *Journal of Physics: Condensed Matter* **18**, 9917 (2006).

[31] C. J. Pickard and R. J. Needs, Structure of phase III of solid hydrogen, *Nature Physics* **3**, 473 (2007).

[32] L. J. Zhang, Y. L. Niu, T. Cui, Y. Li, Y. M. Ma, Z. He, and G. T. Zou, The broken-symmetry phase of

solid hydrogen: Evidence from infrared and raman active vibrons, *Journal of Physics: Condensed Matter* **19**, 425237 (2007).

[33] C. J. Pickard and R. J. Needs, Structures at high pressure from random searching, *physica status solidi (b)* **246**, 536 (2009).

[34] M. Moraldi, Orientational structures in solid para-hydrogen in the broken symmetry phase, *Physical Review B* **80**, 134117 (2009).

[35] X.-Z. Li, B. Walker, M. I. J. Probert, C. J. Pickard, R. J. Needs, and A. Michaelides, Classical and quantum ordering of protons in cold solid hydrogen under megabar pressures, *Journal of Physics: Condensed Matter* **25**, 85402 (2013), arXiv:1302.0062 [cond-mat].

[36] S. Azadi and W. M. C. Foulkes, Fate of density functional theory in the study of high-pressure solid hydrogen, *Physical Review B* **88**, 14115 (2013).

[37] S. Azadi, W. M. C. Foulkes, and T. D. Kühne, Quantum monte carlo study of high pressure solid molecular hydrogen, *New Journal of Physics* **15**, 113005 (2013).

[38] N. D. Drummond, B. Monserrat, J. H. Lloyd-Williams, P. L. Ríos, C. J. Pickard, and R. J. Needs, Quantum monte carlo study of the phase diagram of solid molecular hydrogen at extreme pressures, *Nature Communications* **6**, 7794 (2015).

[39] H. Zong, H. Wiebe, and G. J. Ackland, Understanding high pressure molecular hydrogen with a hierarchical machine-learned potential, *Nature Communications* **11**, 5014 (2020).

[40] M. Hellgren, D. Contant, T. Pitts, and M. Casula, High-pressure II-III phase transition in solid hydrogen: Insights from state-of-the-art ab initio calculations, *Physical Review Research* **4**, L042009 (2022).

[41] C. Li, High-pressure structures of solid hydrogen: Insights from ab initio molecular dynamics simulations, *Journal of Chemical Physics* **160**, 144302 (2024).

[42] S. Biermann, D. Hohl, and D. Marx, Quantum effects in solid hydrogen at ultra-high pressure, *Solid State Communications* **108**, 337 (1998).

[43] G. Geneste, M. Torrent, F. Bottin, and P. Loubeyre, Strong isotope effect in phase II of dense solid hydrogen and deuterium, *Physical Review Letters* **109**, 155303 (2012).

[44] M. Bonitz, J. Vorberger, M. Bethkenhagen, M. P. Böhme, D. M. Ceperley, A. Filinov, T. Gawne, F. Graziani, G. Gregori, P. Hamann, S. B. Hansen, M. Holzmann, S. X. Hu, H. Kähler, V. V. Karasiev, U. Kleinschmidt, L. Kordts, C. Makait, B. Militzer, Z. A. Moldabekov, C. Pierleoni, M. Preising, K. Ramakrishna, R. Redmer, S. Schwalbe, P. Svensson, and T. Dornheim, Toward first principles-based simulations of dense hydrogen, *Physics of Plasmas* **31**, 110501 (2024).

[45] B. Monserrat, R. J. Needs, E. Gregoryanz, and C. J. Pickard, Hexagonal structure of phase III of solid hydrogen, *Physical Review B* **94**, 134101 (2016).

[46] M. A. Morales, J. M. McMahon, C. Pierleoni, and D. M. Ceperley, Towards a predictive first-principles description of solid molecular hydrogen with density functional theory, *Physical Review B* **87**, 184107 (2013).

[47] H. Nagara and T. Nakamura, Stable phases of solid hydrogen at megabar pressures and at zero temperature, *Physical Review Letters* **68**, 2468 (1992).

[48] M. P. Surh, T. W. Barbee, and C. Mailhiot, Zero-point motion and the insulator-metal transition in solid molecular hydrogen, *Physical Review Letters* **70**, 4090 (1993).

[49] G. J. Ackland and J. S. Loveday, Structures of solid hydrogen at 300 K, *Physical Review B* **101**, 94104 (2020).

[50] J. Kohanoff, S. Scandolo, S. de Gironcoli, and E. Tosatti, Dipole-quadrupole interactions and the nature of phase III of compressed hydrogen, *Physical Review Letters* **83**, 4097 (1999).

[51] T. E. Markland and M. Ceriotti, Nuclear quantum effects enter the mainstream, *Nature Reviews Chemistry* **2**, 109 (2018).

[52] H. Niu, Y. Yang, S. Jensen, M. Holzmann, C. Pierleoni, and D. M. Ceperley, Stable solid molecular hydrogen above 900 K from a machine-learned potential trained with diffusion quantum monte carlo, *Physical Review Letters* **130**, 76102 (2023).

[53] T. Cui, E. Cheng, B. J. Alder, and K. B. Whaley, Rotational ordering in solid deuterium and hydrogen: A path integral monte carlo study, *Physical Review B* **55**, 12253 (1997).

[54] E. Kaxiras and Z. Guo, Orientational order in dense molecular hydrogen: A first-principles path-integral monte carlo calculation, *Physical Review B* **49**, 11822 (1994).

[55] M. P. Surh, K. J. Runge, T. W. Barbee, E. L. Pollock, and C. Mailhiot, Ab initio calculations for solid molecular hydrogen, *Physical Review B* **55**, 11330 (1997).

[56] S. Azadi, B. Monserrat, W. M. C. Foulkes, and R. J. Needs, Dissociation of high-pressure solid molecular hydrogen: A quantum monte carlo and anharmonic vibrational study, *Physical Review Letters* **112**, 165501 (2014).

[57] L. Monacelli, M. Casula, K. Nakano, S. Sorella, and F. Mauri, Quantum phase diagram of high-pressure hydrogen, *Nature Physics* **19**, 845 (2023).

[58] G. Carleo and M. Troyer, Solving the quantum many-body problem with artificial neural networks, *Science* **10.1126/science.aag2302** (2017).

[59] D. Pfau, J. S. Spencer, A. G. d. G. Matthews, and W. M. C. Foulkes, Ab-initio solution of the many-electron schrödinger equation with deep neural networks, *Physical Review Research* **2**, 33429 (2020), arXiv:1909.02487 [physics].

[60] J. Hermann, J. Spencer, K. Choo, A. Mezzacapo, W. M. C. Foulkes, D. Pfau, G. Carleo, and F. Noé, Ab initio quantum chemistry with neural-network wavefunctions, *Nature Reviews Chemistry* **7**, 692 (2023).

[61] Y. Qian, X. Li, Z. Li, W. Ren, and J. Chen, Deep Learning Quantum Monte Carlo for Solids, *WIREs Computational Molecular Science* **15**, e70015 (2025).

[62] J. Han, L. Zhang, and W. E, Solving many-electron schrödinger equation using deep neural networks, *Journal of Computational Physics* **399**, 108929 (2019).

[63] J. Hermann, Z. Schätzle, and F. Noé, Deep-neural-network solution of the electronic schrödinger equation, *Nature Chemistry* **12**, 891 (2020).

[64] D. Pfau, S. Axelrod, H. Sutterud, I. von Glehn, and J. S. Spencer, Accurate computation of quantum excited states with neural networks, *Science* **385**, eadn0137 (2024).

[65] A. Foster, Z. Schätzle, P. B. Szabó, L. Cheng, J. Köhler, G. Cassella, N. Gao, J. Li, F. Noé, and J. Hermann, An ab initio foundation model of wavefunctions that

accurately describes chemical bond breaking (2025), arXiv:2506.19960 [physics].

[66] R. Li, Y. Liu, D. Jiang, Y. Chen, X. Wen, W. Li, D. He, L. Wang, J. Chen, and W. Ren, *Spin-Adapted Neural Network Wavefunctions in Real Space* (2025), arXiv:2511.01671 [physics].

[67] X. Li, Z. Li, and J. Chen, Ab initio calculation of real solids via neural network ansatz, *Nature Communications* **13**, 1 (2022).

[68] X. Li, Y. Qian, W. Ren, Y. Xu, and J. Chen, Emergent wigner phases in moiré superlattice from deep learning (2024), arXiv:2406.11134 [physics].

[69] D. Luo, D. D. Dai, and L. Fu, *Simulating moiré quantum matter with neural network* (2024), arXiv:2406.17645.

[70] G. Cassella, H. Sutterud, S. Azadi, N. D. Drummond, D. Pfau, J. S. Spencer, and W. M. C. Foulkes, Discovering quantum phase transitions with fermionic neural networks, *Physical Review Letters* **130**, 36401 (2023).

[71] G. Pescia, J. Nys, J. Kim, A. Lovato, and G. Carleo, Message-passing neural quantum states for the homogeneous electron gas, *Physical Review B* **110**, 035108 (2024).

[72] C. Smith, Y. Chen, R. Levy, Y. Yang, M. A. Morales, and S. Zhang, Unified Variational Approach Description of Ground-State Phases of the Two-Dimensional Electron Gas, *Physical Review Letters* **133**, 266504 (2024).

[73] A. Valenti, V. Calvera, Y. Yang, M. A. Morales, S. A. Kivelson, I. Esterlis, and S. Zhang, Critical Gate Distance for Wigner Crystallization in the Two-Dimensional Electron Gas, *Physical Review Letters* **135**, 166501 (2025).

[74] Z. Ge, C. Smith, Z. He, Y. Yang, Q. Li, Z. Xiang, J. Xiao, W. Zhou, S. Kahn, M. Erdi, R. Banerjee, T. Taniguchi, K. Watanabe, S. A. Tongay, M. A. Morales, S. Zhang, F. Wang, and M. F. Crommie, *Visualizing the Impact of Quenched Disorder on 2D Electron Wigner Solids* (2025), arXiv:2510.12009 [cond-mat].

[75] C.-T. Li, T. Ong, M. Geier, H. Lin, and L. Fu, *Attention is all you need to solve chiral superconductivity* (2025), arXiv:2509.03683 [cond-mat].

[76] D. Luo, D. D. Dai, and L. Fu, Pairing-based graph neural network for simulating quantum materials (2023), arXiv:2311.02143 [cond-mat, physics:physics, physics:quant-ph].

[77] W. T. Lou, H. Sutterud, G. Cassella, W. M. C. Foulkes, J. Knolle, D. Pfau, and J. S. Spencer, Neural wave functions for superfluids, *Physical Review X* **14**, 21030 (2024).

[78] H. Xie, Z.-H. Li, H. Wang, L. Zhang, and L. Wang, Deep Variational Free Energy Approach to Dense Hydrogen, *Physical Review Letters* **131**, 126501 (2023).

[79] X. Dong, H. Xie, Y. Chen, W. Liang, L. Zhang, L. Wang, and H. Wang, Deep variational free energy prediction of dense hydrogen solid at 1200 K, *Physical Review B* **111**, 214118 (2025).

[80] D. Linteau, S. Moroni, G. Carleo, and M. Holzmann, *Universal neural wave functions for high-pressure hydrogen* (2025), arXiv:2504.07062 [cond-mat].

[81] Y. Qian, T. Zhao, J. Zhang, T. Xiang, X. Li, and J. Chen, Describing landau level mixing in fractional quantum hall states with deep learning, *Physical Review Letters* **134**, 176503 (2025).

[82] Y. Teng, D. D. Dai, and L. Fu, Solving the fractional quantum hall problem with self-attention neural network, *Physical Review B* **111**, 205117 (2025).

[83] M. Gattu, *Dressing composite fermions with artificial intelligence* (2025), arXiv:2512.00527 [cond-mat].

[84] A. Abouelkomsan, M. Geier, and L. Fu, *Topological Order in Deep State* (2025), arXiv:2512.01863 [cond-mat].

[85] X. Li, Y. Chen, B. Li, H. Chen, F. Wu, J. Chen, and W. Ren, *Deep learning sheds light on integer and fractional topological insulators* (2025), arXiv:2503.11756 [cond-mat].

[86] D. Linteau, G. Pescia, J. Nys, G. Carleo, and M. Holzmann, Phase diagram and crystal melting of helium-4 in two dimensions, *Physical Review Letters* **134**, 246001 (2025).

[87] E. Wang, *Full Quantum Effects in Condensed Matter Physics: Beyond the Born-Oppenheimer Approximation* (Cambridge University Press, Cambridge, 2025).

[88] M. Born, K. Huang, and M. Lax, *Dynamical Theory of Crystal Lattices*, *American Journal of Physics* **23**, 474 (1955).

[89] A. Abedi, N. T. Maitra, and E. K. U. Gross, Exact Factorization of the Time-Dependent Electron-Nuclear Wave Function, *Physical Review Letters* **105**, 123002 (2010).

[90] G. Hunter, Conditional probability amplitudes in wave mechanics, *International Journal of Quantum Chemistry* **9**, 237 (1975).

[91] V. Natoli, R. M. Martin, and D. M. Ceperley, Crystal structure of atomic hydrogen, *Physical Review Letters* **70**, 1952 (1993).

[92] I. F. Silvera, The solid molecular hydrogens in the condensed phase: Fundamentals and static properties, *Reviews of Modern Physics* **52**, 393 (1980).

[93] I. F. Silvera, The Validity of Ortho and Para States of Hydrogen at Megabar Pressures, *Journal of Low Temperature Physics* **112**, 237 (1998).

[94] T. Bachlechner, B. P. Majumder, H. H. Mao, G. W. Cottrell, and J. McAuley, *Rezero is all you need: Fast convergence at large depth* (2020), arXiv:2003.04887 [cs.LG].

[95] T. M. Whitehead, M. H. Michael, and G. J. Conduit, Jastrow correlation factor for periodic systems, *Physical Review B* **94**, 35157 (2016).

[96] M. Lundy and A. Mees, Convergence of an annealing algorithm, *Mathematical Programming* **34**, 111 (1986).

[97] D. M. Ceperley and M. Dewing, The penalty method for random walks with uncertain energies, *Journal of Chemical Physics* **110**, 9812 (1999), arXiv:physics/9812035.

[98] See Fig. S1 and related discussion.

[99] D. M. Ceperley and B. J. Alder, Ground state of solid hydrogen at high pressures, *Physical Review B* **36**, 2092 (1987).

[100] V. Natoli, R. M. Martin, and D. Ceperley, Crystal structure of molecular hydrogen at high pressure, *Physical Review Letters* **74**, 1601 (1995).

[101] X. W. Wang, J. Zhu, S. G. Louie, and S. Fahy, Magnetic structure and equation of state of bcc solid hydrogen: A variational quantum monte carlo study, *Physical Review Letters* **65**, 2414 (1990).

[102] M. Holzmann, D. M. Ceperley, C. Pierleoni, and K. Esler, Backflow correlations for the electron gas and metallic hydrogen, *Physical Review E* **68**, 46707 (2003).

[103] C. Attaccalite and S. Sorella, Stable liquid hydrogen at high pressure by a novel *ab initio* molecular-dynamics calculation, *Physical Review Letters* **100**,

114501 (2008).

[104] C. Pierleoni, K. T. Delaney, M. A. Morales, D. M. Ceperley, and M. Holzmann, Trial wave functions for high-pressure metallic hydrogen, *Computer Physics Communications* **179**, 89 (2008), arXiv:0712.0161 [physics].

[105] M. Holzmann, C. Pierleoni, and D. M. Ceperley, Coupled Electron–Ion Monte Carlo calculations of atomic hydrogen, .

[106] P. Tolédano, H. Katzke, A. F. Goncharov, and R. J. Hemley, Symmetry breaking in dense solid hydrogen: Mechanisms for the transitions to phase II and phase III, *Physical Review Letters* **103**, 105301 (2009).

[107] L. Cui, N. H. Chen, and I. F. Silvera, Excitations, order parameters, and phase diagram of solid deuterium at megabar pressures, *Physical Review B* **51**, 14987 (1995).

[108] H.-k. Mao and R. J. Hemley, Ultrahigh-pressure transitions in solid hydrogen, *Reviews of Modern Physics* **66**, 671 (1994).

[109] S. Gorai, P. Modak, and A. K. Verma, *Ab-initio* study of $C2/c$, $Cmca-12$, $Pbcn$ and $P6122$ phases of solid hydrogen, *Physica B: Condensed Matter* **655**, 414772 (2023).

[110] I. Errea, F. Belli, L. Monacelli, A. Sanna, T. Koretsune, T. Tadano, R. Bianco, M. Calandra, R. Arita, F. Mauri, and J. A. Flores-Livas, Quantum crystal structure in the 250-kelvin superconducting lanthanum hydride, *Nature* **578**, 66 (2020).

[111] B. Monserrat, N. D. Drummond, P. Dalladay-Simpson, R. T. Howie, P. López Ríos, E. Gregoryanz, C. J. Pickard, and R. J. Needs, Structure and Metallicity of Phase V of Hydrogen, *Physical Review Letters* **120**, 255701 (2018).

[112] K. Nakamoto, *Infrared and Raman Spectra of Inorganic and Coordination Compounds*, 6th ed. (Wiley, Hoboken, N.J, 2009).

Supplemental Material for Revisiting the broken symmetry phase of Solid Hydrogen: A Neural-Network Variational Monte Carlo Study

Shengdu Chai^{1,2}, Chen Lin³, Xinyang Dong⁴, Yuqiang Li²,
Wanli Ouyang^{2,5}, Lei Wang⁴, and X.C. Xie^{1,6,7}

¹*Interdisciplinary Center for Theoretical Physics and Information Sciences (ICTPIS), Fudan University, Shanghai 200433, China*

²*Shanghai Artificial Intelligence Laboratory, Shanghai 200232, China*

³*Department of Engineering, University of Oxford, Oxford OX1 4BH, UK*

⁴*Beijing National Laboratory for Condensed Matter Physics and Institute of Physics, Chinese Academy of Sciences, Beijing 100190, China*

⁵*Department of Information Engineering, The Chinese University of Hong Kong, Hong Kong SAR HKG, China*

⁶*International Center for Quantum Materials, School of Physics, Peking University, Beijing 100871, China*

⁷*Hefei National Laboratory, Hefei 230088, China*

I. NEURAL NETWORK WAVEFUNCTION

To satisfy the PBCs required by the simulation cell, we map Cartesian coordinates to periodic descriptors via fractional coordinates [70]. Let $\mathbf{r}_{ij} = \mathbf{r}_i - \mathbf{r}_j$ be a relative displacement vector. We decompose this vector into the lattice basis $\{\mathbf{a}_k\}$ as $\mathbf{r}_{ij} = \sum_{k=1}^3 \omega_{ij,k} \mathbf{a}_k$. The periodic distance is computed using the lattice metric tensor $S_{kl} = \mathbf{a}_k \cdot \mathbf{a}_l$ as:

$$d(\mathbf{r}) = \left[(1 - \cos \omega_k) S_{kl} (1 - \cos \omega_l) + \sin \omega_k S_{kl} \sin \omega_l \right]^{1/2}. \quad (\text{S1})$$

The input feature vectors $\mathbf{h}_{\alpha\beta}^1$ for the first neural network layer are constructed by concatenating the periodic embedding of relative positions with this distance metric:

$$\mathbf{h}_{\alpha\beta}^1 = \left\{ \sum_k \sin(\omega_{\alpha\beta}^k) \mathbf{a}_k, \sum_k \cos(\omega_{\alpha\beta}^k) \mathbf{a}_k, d(\omega_{\alpha\beta}) \right\}, \quad (\text{S2})$$

where α, β denote any pair of particles (electron-electron, nucleus-nucleus, or electron-nucleus).

The pseudocode for the nuclear wavefunction and electron wavefunction is given in [Algorithm 1](#) and [Algorithm 2](#), respectively. As for the sampling algorithm, the two-stage Gibbs sampler is summarized in [Algorithm 3](#), with the original one-shot Metropolis scheme provided for reference in [Algorithm 4](#)

Algorithm 1. Pseudocode of $\ln \chi(\mathbf{R})$ for nuclear wavefunction

```

1: Input: nuclear positions  $\{\mathbf{R}_I\}$ 
2: Input: lattice vector  $\{\mathbf{a}_1, \mathbf{a}_2, \mathbf{a}_3\}$  of simulation cell
3: Input: reciprocal lattice vector  $\{\mathbf{b}_1, \mathbf{b}_2, \mathbf{b}_3\}$  of simulation cell
4: Output: log of nuclear wavefunction  $\ln \chi(\mathbf{R})$ 
5: for each atom  $I, J$  do
6:    $\omega_{IJ}^k = (\mathbf{R}_I - \mathbf{R}_J) \cdot \mathbf{b}_k$ 
7: end for
8: for each atom  $I, J$  do
9:    $\mathbf{h}_{I,J}^1 = \{\sum_k \sin(\omega_{IJ}^k) \mathbf{a}_k, \sum_k \cos(\omega_{IJ}^k) \mathbf{a}_k, d(\omega_{IJ})\}$ 
10: end for
11: for each layer  $l$  do
12:    $\mathbf{h}_{IJ}^{l+1} = \tanh(\mathbf{\Pi}_{\text{atom}}^l \cdot \mathbf{h}_{IJ}^l + \mathbf{c}_{\text{atom}}^l)$ 
13:    $\mathbf{h}_{IJ}^{l+1} = \frac{1}{\sqrt{2}}(\mathbf{h}_{IJ}^l + \mathbf{h}_{IJ}^{l+1})$  ▷ Residual connection
14: end for
15:  $\mathbf{d}_{IJ}^{\text{pred}} = \mathbf{\Pi}_{\text{atom}}^{\text{dist}} \cdot \mathbf{h}_{IJ}^L + \mathbf{c}_{\text{atom}}^{\text{dist}}$  ▷ Shape (natom, natom, 1)
16:  $d_{IJ}^{\text{env}} = \alpha * \mathbf{d}_{IJ}^{\text{pred}} + d(\omega_{IJ})$  ▷ Rezero
17:  $\ln \chi(\mathbf{R}) = - \sum_{IJ} \sigma_{IJ}^2 (d_{IJ}^{\text{env}} - b_{IJ})^2$  ▷ b is param of network

```

Algorithm 2. Pseudocode of electron wavefunction

```

1: Input: electron positions  $\{\mathbf{r}_1^\uparrow, \dots, \mathbf{r}_{n\uparrow}^\uparrow, \mathbf{r}_1^\downarrow, \dots, \mathbf{r}_{n\downarrow}^\downarrow\}$ 
2: Input: nuclear positions  $\{\mathbf{R}_I\}$  in the simulation cell
3: Input: lattice vector  $\{\mathbf{a}_1, \mathbf{a}_2, \mathbf{a}_3\}$  of simulation cell
4: Input: reciprocal lattice vector  $\{\mathbf{b}_1, \mathbf{b}_2, \mathbf{b}_3\}$  of simulation cell
5: Input: occupied  $\{\mathbf{k}_i\}$ 
6: Output: wavefunction ansatz  $\varphi(\mathbf{r}, \mathbf{R})$ 
7: for each electron  $i, j$ , atom  $I$  do
8:    $\omega_{iI}^k = (\mathbf{r}_i - \mathbf{R}_I) \cdot \mathbf{b}_k$ ,
9:    $\omega_{ij}^k = (\mathbf{r}_i - \mathbf{r}_j) \cdot \mathbf{b}_k$ 
10: end for
11: for each electron  $i, j$ , atom  $I$  do
12:    $\mathbf{h}_{i,I}^1 = \{\sum_k \sin(\omega_{iI}^k) \mathbf{a}_k, \sum_k \cos(\omega_{iI}^k) \mathbf{a}_k, d(\omega_{iI})\}$ 
13:    $\mathbf{h}_{i,j}^1 = \{\sum_k \sin(\omega_{ij}^k) \mathbf{a}_k, \sum_k \cos(\omega_{ij}^k) \mathbf{a}_k, d(\omega_{ij})\}$ 
14: end for
15: for each layer  $l$  do
16:    $\mathbf{g}_{i,I}^{l,\uparrow} = \frac{1}{n\uparrow} \sum_i \mathbf{h}_{i,I}^{l,\uparrow}$ 
17:    $\mathbf{g}_{i,I}^{l,\downarrow} = \frac{1}{n\downarrow} \sum_i \mathbf{h}_{i,I}^{l,\downarrow}$ 
18:   for each electron  $i$ , spin  $\alpha$  do
19:      $\mathbf{g}_i^{l,\alpha,\uparrow} = \frac{1}{n\uparrow} \sum_j \mathbf{h}_{i,j}^{l,\alpha,\uparrow}$ 
20:      $\mathbf{g}_i^{l,\alpha,\downarrow} = \frac{1}{n\downarrow} \sum_j \mathbf{h}_{i,j}^{l,\alpha,\downarrow}$ 
21:      $\mathbf{f}_i^{l,\alpha} = \text{concat}(\mathbf{h}_i^{l,\alpha}, \mathbf{g}_{i,I}^{l,\uparrow}, \mathbf{g}_{i,I}^{l,\downarrow}, \mathbf{g}_i^{l,\alpha,\uparrow}, \mathbf{g}_i^{l,\alpha,\downarrow})$ 
22:      $\mathbf{h}_i^{l+1,\alpha} = \tanh(V^l \cdot \mathbf{f}_i^{l,\alpha} + \mathbf{b}^l) + \mathbf{h}_i^{l,\alpha}$ 
23:      $\mathbf{h}_{i,j}^{l+1,\alpha,\beta} = \tanh(W^l \cdot \mathbf{h}_{i,j}^{l,\alpha,\beta} + \mathbf{c}^l) + \mathbf{h}_{i,j}^{l,\alpha,\beta}$ 
24:   end for
25: end for
26: for each electron  $i, j, \text{spin } \alpha$  do
27:    $u_{\mathbf{k}_i}^\alpha(\mathbf{r}_j; \mathbf{r}_{\neq j}) = \text{Orb}_{j,\alpha}^{Re} \mathbf{h}_{i,I}^L + i \text{Orb}_{j,\alpha}^{Im} \mathbf{h}_{i,I}^L$ 
28:    $p_{i,j}^\alpha = \exp(i \mathbf{k}_i \cdot \mathbf{r}_j^\alpha)$ 
29:    $\text{env}_{i,j}^\alpha = \sum_I \pi_{i,I}^\alpha \exp[-\sigma_{i,I}^\alpha d(\omega_{i,I})]$ 
30:    $\phi_{i,j}^\alpha = p_{i,j}^\alpha u_{\mathbf{k}_i}^\alpha(\mathbf{r}_j; \mathbf{r}_{\neq j}) \text{env}_{i,j}^\alpha$ 
31: end for
32:  $\varphi(\mathbf{r}, \mathbf{R}) = \text{Det}[\phi^\uparrow] \text{Det}[\phi^\downarrow]$ 

```

II. ENTHALPY OPERATOR AND COORDINATE MAP

Rather than treating lattice parameters as variational degrees of freedom in Ψ , we incorporate them into the enthalpy operator and sample in unit-scaled (fractional) coordinates [86]. We define the set of all real-space particle coordinates as $\mathcal{X} = \{\mathbf{r}_i\} \cup \{\mathbf{R}_I\}$ and the corresponding set of fractional coordinates as $\mathcal{S} = \{\mathbf{s}_i\} \cup \{\mathbf{S}_I\}$, where all $\mathbf{s}_i, \mathbf{S}_I \in [0, 1]^3$. The mapping from fractional to real coordinates is given by $\mathcal{X} = L^\top \mathcal{S}$, where L is the lattice matrix and $L^\top \mathcal{S} = (L^\top s_1, \dots, L^\top s_N, L^\top S_1, \dots, L^\top S_N)$. Defining $g = LL^\top$ and $g^{-1} = (L^{-1})^\top L^{-1}$, the local estimator becomes,

$$\begin{aligned}
G_{\text{loc}}(\mathcal{S}) &= K_{\text{loc}}(\mathcal{S}) + V_{\text{loc}}(\mathcal{S}) \\
K_{\text{loc}}(\mathcal{S}) &= - \sum_p \frac{1}{2m_p} \left[\sum_{\alpha, \beta} g_{\alpha, \beta}^{-1} \frac{\partial^2}{\partial s_p^\alpha \partial s_p^\beta} \ln \Psi(\mathcal{S}) \right. \\
&\quad \left. + (L^{-1} \nabla_{s_p} \ln \Psi(\mathcal{S}))^2 \right] \\
V_{\text{loc}}(\mathcal{S}) &= V(L^\top \mathcal{S}) + P\Omega = V(L^\top \mathcal{S}) + P \det L
\end{aligned} \tag{S3}$$

Algorithm 3. Gibbs Block Sampling for Joint Electron-Nucleus Configuration

```

1: Input: initial electron positions  $\mathbf{r}^{(0)}$ 
2: Input: initial nuclear positions  $\mathbf{R}^{(0)}$ 
3: Input: unnormalized probability density  $p(\mathbf{r}, \mathbf{R}) = |\Psi(\mathbf{r}, \mathbf{R})|^2$ 
4: Input: proposal distributions  $q(\mathbf{R}|\hat{\mathbf{R}})$ ,  $q(\mathbf{r}|\hat{\mathbf{r}})$ 
5: Input: number of iterations  $T$ 
6: Input: number of blocks  $B$ 
7: Output: samples  $\{\mathbf{R}^{(t)}, \mathbf{r}^{(t)}\} \sim p(\mathbf{R}, \mathbf{r})$ 
8: Initialize  $\mathbf{r}_{\text{prev}} \leftarrow \mathbf{r}^{(0)}$ ,  $\mathbf{R}_{\text{prev}} \leftarrow \mathbf{R}^{(0)}$ 
9: for  $b = 1$  to  $B$  do
10:   for  $\tau = 1$  to  $T$  do
11:     Propose  $\mathbf{R}^* \sim q(\mathbf{R}|\mathbf{R}_{\text{prev}})$ 
12:     Draw  $u \sim \mathcal{U}(0, 1)$ 
13:     Compute acceptance ratio  $\alpha = \frac{p(\mathbf{R}^*|\mathbf{r}_{\text{prev}})}{p(\mathbf{R}_{\text{prev}}|\mathbf{r}_{\text{prev}})}$ 
14:     if  $u < \alpha$  then
15:        $\mathbf{R}_{\text{prev}} \leftarrow \mathbf{R}^*$ 
16:     end if
17:   end for
18:   for  $\tau = 1$  to  $T$  do
19:     Propose  $\mathbf{r}^* \sim q(\mathbf{r}|\mathbf{r}_{\text{prev}})$ 
20:     Draw  $u \sim \mathcal{U}(0, 1)$ 
21:     Compute acceptance ratio  $\alpha = \frac{p(\mathbf{r}^*|\mathbf{R}_{\text{prev}})}{p(\mathbf{r}_{\text{prev}}|\mathbf{R}_{\text{prev}})}$ 
22:     if  $u < \alpha$  then
23:        $\mathbf{r}_{\text{prev}} \leftarrow \mathbf{r}^*$ 
24:     end if
25:   end for
26: end for
27: Record:  $\mathbf{R}^{(t)} \leftarrow \mathbf{R}_{\text{prev}}$ ,  $\mathbf{r}^{(t)} \leftarrow \mathbf{r}_{\text{prev}}$ 

```

Algorithm 4. Metropolis Sampling for Joint Electron-Nucleus Configuration

```

1: Input: initial electron positions  $\mathbf{r}^{(0)}$ 
2: Input: initial nuclear positions  $\mathbf{R}^{(0)}$ 
3: Input: unnormalized probability density  $p(\mathbf{r}, \mathbf{R}) = |\Psi(\mathbf{r}, \mathbf{R})|^2$ 
4: Input: proposal distributions  $q(\mathbf{R}|\hat{\mathbf{R}})$ ,  $q(\mathbf{r}|\hat{\mathbf{r}})$ 
5: Input: number of iterations  $T$ 
6: Output: samples  $\{\mathbf{R}^{(t)}, \mathbf{r}^{(t)}\} \sim p(\mathbf{r}, \mathbf{R})$ 
7: Initialize  $\mathbf{r}_{\text{prev}} \leftarrow \mathbf{r}^{(0)}$ ,  $\mathbf{R}_{\text{prev}} \leftarrow \mathbf{R}^{(0)}$ 
8: for  $\tau = 1$  to  $t$  do
9:   Propose  $\mathbf{r}^* \sim q(\mathbf{r}|\mathbf{r}_{\text{prev}})$ 
10:  Propose  $\mathbf{R}^* \sim q(\mathbf{R}|\mathbf{R}_{\text{prev}})$ 
11:  Draw  $u \sim \mathcal{U}(0, 1)$ 
12:  Compute acceptance ratio  $\alpha = \frac{p(\mathbf{r}^*, \mathbf{R}^*)}{p(\mathbf{r}_{\text{prev}}, \mathbf{R}_{\text{prev}})}$ 
13:  if  $u < \alpha$  then
14:     $\mathbf{r}_{\text{prev}} \leftarrow \mathbf{r}^*$ ,  $\mathbf{R}_{\text{prev}} \leftarrow \mathbf{R}^*$ 
15:  end if
16: end for
17: Record:  $\mathbf{r}^{(t)} \leftarrow \mathbf{r}_{\text{prev}}$ ,  $\mathbf{R}^{(t)} \leftarrow \mathbf{R}_{\text{prev}}$ 

```

where $m_p = \begin{cases} 1, & p \leq N \\ M, & N < p \leq 2N \end{cases}$. The lattice is characterized by six parameters $(a, b, c, \alpha, \beta, \gamma)$, with a, b, c the lengths of the three basis vectors and α, β, γ the angles between them. The lattice matrix L is written as

$$L = \begin{pmatrix} a & 0 & 0 \\ b \cos \gamma & b \sin \gamma & 0 \\ c \cos \beta & -c \sin \beta \cos \alpha^* & c \sin \beta \sin \alpha^* \end{pmatrix}, \quad \cos \alpha^* = \frac{\cos \beta \cos \gamma - \cos \alpha}{\sin \beta \sin \gamma}. \quad (\text{S4})$$

For clarity, we assume the wavefunction in the NVT ensemble has the form $\Psi_{\theta \cup L_{\text{fixed}}}(\mathcal{X})_{\text{NVT}}$. The NPT wavefunction is defined via the NVT form in the unit cube,

$$\Psi_{\theta}(\mathcal{S})_{\text{NPT}} \equiv \Psi_{\theta \cup L=I}(\mathcal{S})_{\text{NVT}}. \quad (\text{S5})$$

so that geometry enters only through the operator and coordinate map.

III. BEYOND BO ENERGY

The trial wave function can be expressed as:

$$\Psi(\mathbf{r}, \mathbf{R}) = \chi(\mathbf{R}) \varphi(\mathbf{r}, \mathbf{R}), \quad (\text{S6})$$

The local energy is given by:

$$\begin{aligned} E_{\text{loc}} &= \frac{\hat{H}\Psi(\mathbf{r}, \mathbf{R})}{\Psi(\mathbf{r}, \mathbf{R})} \\ &= -\frac{1}{2M} \sum_{I=1}^N \frac{\nabla_{\mathbf{R}_I}^2 \Psi(\mathbf{r}, \mathbf{R})}{\Psi(\mathbf{r}, \mathbf{R})} - \frac{1}{2} \sum_{i=1}^N \frac{\nabla_{\mathbf{r}_i}^2 \Psi(\mathbf{r}, \mathbf{R})}{\Psi(\mathbf{r}, \mathbf{R})} + V(\mathbf{r}, \mathbf{R}) \\ &= -\frac{1}{2M} \sum_{I=1}^N \left(\frac{\nabla_{\mathbf{R}_I}^2 \chi(\mathbf{R})}{\chi(\mathbf{R})} + \frac{\nabla_{\mathbf{R}_I}^2 \varphi(\mathbf{r}, \mathbf{R})}{\varphi(\mathbf{r}, \mathbf{R})} + 2\nabla_{\mathbf{R}_I} \varphi(\mathbf{r}, \mathbf{R}) \cdot \nabla_{\mathbf{R}_I} \chi(\mathbf{R}) \right) - \frac{1}{2} \sum_{i=1}^N \frac{\nabla_{\mathbf{r}_i}^2 \Psi(\mathbf{r}, \mathbf{R})}{\Psi(\mathbf{r}, \mathbf{R})} + V(\mathbf{r}, \mathbf{R}) \end{aligned} \quad (\text{S7})$$

The terms in red denote the beyond BO contributions to the local energy which is captured by the present calculation. So we can define the nuclear kinetic energy under the BO approximation (K_{BO}) and the beyond BO correction ($K_{\text{non-BO}}$) as the expectation of the blue and red term respectively.

IV. TRAINING PARAMETERS AND TRAINING CURVES

Table I lists the hyperparameters for the benchmark calculation of a dynamic BCC lattice at $r_s = 1.31$ in the NVT ensemble, while Table II details those for various initial structures in the broken symmetry phase under the NPT ensemble. For the NPT training, we adopted a multi-stage strategy comprising three parts: (1) Warmup, where lattice parameters are fixed and wavefunction parameters are optimized to establish a high-quality initial wavefunction; (2) Lattice training, where wavefunction parameters are frozen while lattice parameters are optimized; and (3) Wavefunction training, which mirrors the warmup phase but involves fewer steps. The overall protocol begins with the initial Warmup phase, followed by an alternating cycle of Lattice training and Wavefunction training.

To demonstrate that noise may be beneficial in the simulated annealing process, Fig. S1 compares the training curves of two distinct annealing strategies: (i) a low-noise scheme that averages 10 independent enthalpy estimates per step, and (ii) a high-noise scheme that uses a single estimate but allows for 10 times as many steps. By design, the total computational cost for enthalpy evaluation remains identical for both methods. The results indicate that while both strategies converge to approximately the same enthalpy, the high-noise strategy exhibits faster convergence and yields lower variance. This demonstrates that the statistical noise of the enthalpy estimator supplies an effective stochastic driving force that enhances barrier crossing and accelerates convergence.

In Fig. S2, the left panel displays the training curves for the BCC dynamic lattice at $r_s = 1.31$ within the NVT ensemble. Here, we benchmark our approach against other VMC methods, including NQS and traditional DMC, the latter of which serves as the lowest-energy reference in traditional methods. The right panel illustrates the training curves for various initial structures at $P_{\text{ext}} = 130$ GPa within the NPT ensemble ($P2_1/c$ is first training at $P_{\text{ext}} = 10$ GPa, and then at 130 GPa). These results identify the $Cmcm$ phase as the lowest-energy structure at this pressure. The final enthalpies based on inference with 10000 steps after training are summarized in Table III. The structure with the lowest enthalpy is listed in Table IV.

In Fig. S3, we present the evolution of the lattice parameters and the volume per atom as a function of the training steps. For simplicity, the lattice angles were fixed at $\alpha = \beta = \gamma = 90^\circ$ in Eq. S4 throughout the training, and allowing them to relax produces no appreciable deviation from this constraint as shown in Fig. S4.

TABLE I. Hyperparameters for BCC Train

Hyperparameter	Value	Hyperparameter	Value
Dimension of one-electron layer	256	Dimension of two-electron layer	32
Dimension of nuclear layer	32	Number of layers	3
Number of determinants	16	Optimizer	KFAC
Learning rate	3e-2	Learning rate decay	1
Learning rate delay	1e4	Damping	1e-3
Momentum of optimizer	0.0	Batch size	1024
Number of training steps	6e5	GBS burn in	100
Number of GBS blocks	5	Number of GBS iterations	10
Electron move width	2e-2	Nuclear move width	2e-4
Adapt frequency	100	Precision	Float32

TABLE II. Hyperparameters for Broken Symmetry Phase

Hyperparameter	Value	Hyperparameter	Value
Dimension of one-electron layer	256	Dimension of two-electron layer	32
Dimension of nuclear layer	32	Number of layers	3
Number of determinants	8	Optimizer	KFAC
Learning rate	3e-3	Learning rate decay	1
Learning rate delay	1e4	Damping	1e-3
Momentum of optimizer	0.0	Batch size	1024
Number of training steps ^a	5e5	GBS burn in	100
Number of GBS blocks	10	Number of GBS iterations	10
Electron move width	2e-2	Nuclear move width	2e-4
Adapt frequency	100	Precision	Float32
Beta in Annealing	0.002	Initial virtual temperature	0.1
Annealing steps between each training steps	10	Lattice move width	0.02
Warmup steps	50000	Lattice steps	300
Wavefunction steps	5000	Initial r_s	2.11

^a For $P2_1c$, the number of training steps is 1.2e6

V. XRD ANALYSIS OF CANDIDATE STRUCTURES

Figure S5 displays the structures analyzed in the XRD patterns of Fig. 4. The $P2_1/c$ -8 and $P2_1/c$ -24 phases were taken from Refs. [41] and [33], respectively, with all other structures taken from Ref. [31]. A DFT variable-cell relaxation was performed to obtain the structural parameters at 130 GPa.

TABLE III. Final enthalpies based on inference with 10000 steps after training

Initial Structure	Final Enthalpy (Ha/atom)
$Cmcm$	-0.483666(10)
$Pca2_1$	-0.482817(9)
$P2_1c$	-0.482795(9)
$P6_3/mmc$ with aligned molecule	-0.47791(1)
$P6_3m$	-0.46987(2)

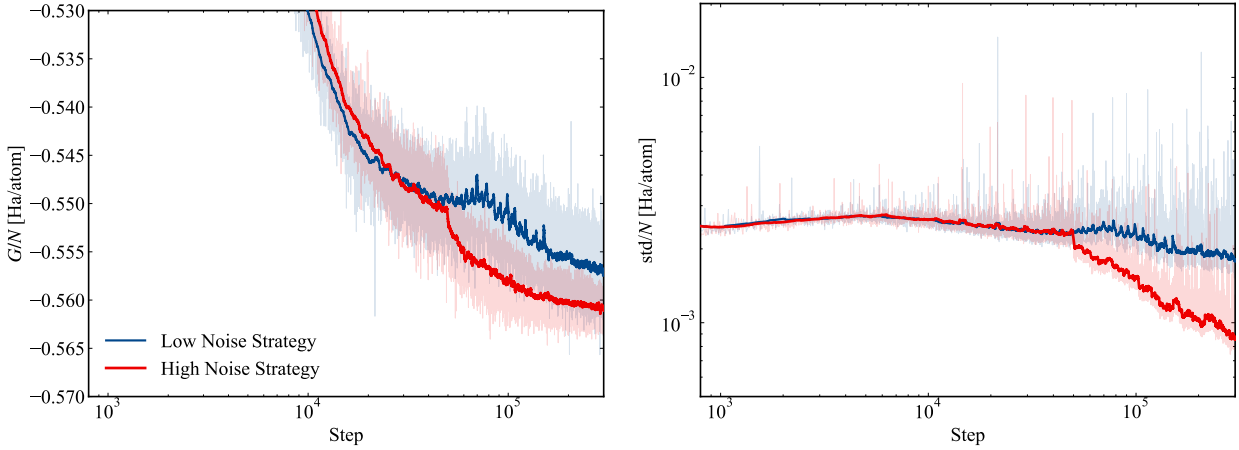


FIG. S1. Comparison of different annealing strategies. The high-noise strategy (single estimate, more steps) demonstrates faster convergence and lower variance compared to the low-noise strategy (averaged estimates), despite identical computational costs. The shadow in the figure represents the original data points, while the solid line is the smoothed curve via a moving average with a window size of 1000 steps.

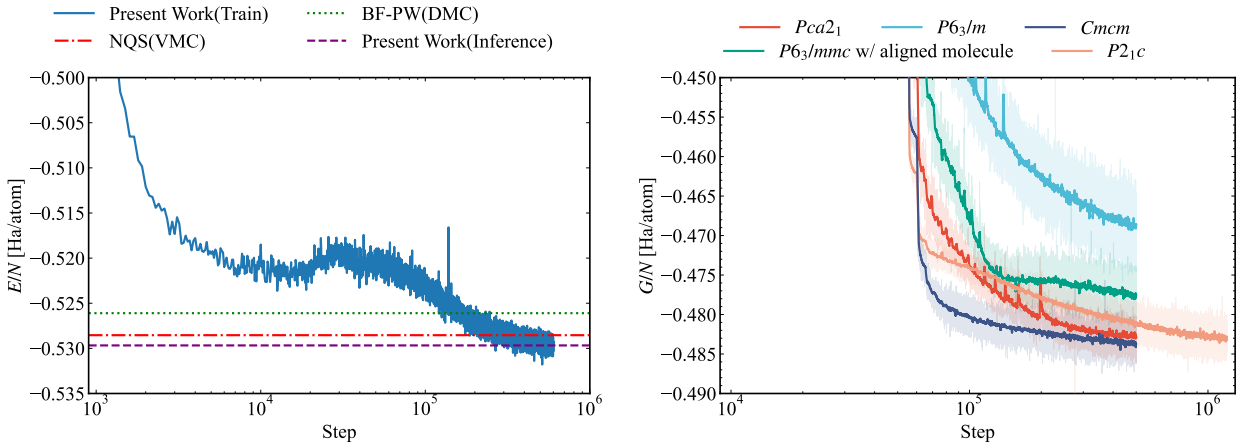


FIG. S2. **Left:** Training curves for the BCC dynamic lattice at $r_s = 1.31$ in the NVT ensemble. **Right:** Training curves for various initial structures at $P_{ext} = 130$ GPa in the NPT ensemble, highlighting the stability of the $Cmcm$ structure. The legend denotes the initial structure. The shadow in the figure represents the original data points, while the solid line is the smoothed curve via a moving average with a window size of 1000 steps.

VI. RAMAN AND IR ANALYSIS

This analysis uses the correlation method [112] to determine the vibrational properties of solid hydrogen. The isolated H_2 molecule belongs to the linear $D_{\infty h}$ point group. In the solid state, hydrogen crystallizes in the orthorhombic space group $Cmcm$, which corresponds to the factor group D_{2h} . The molecular centers of mass occupy three distinct Wyckoff positions: two $4c$ sites and one $8g$ site. The site symmetries for these molecular centers are C_{2v} for the $4c$ positions and C_s for the $8g$ positions. The derivation of the Raman and IR active modes proceeds by:

1. characterizing the modes of the isolated H_2 molecule;
2. constructing correlation tables linking $D_{\infty h}$ to the site symmetries C_{2v} and C_s ;
3. correlating these site symmetries with the factor group D_{2h} ; and
4. deriving the selection rules for the crystal lattice.

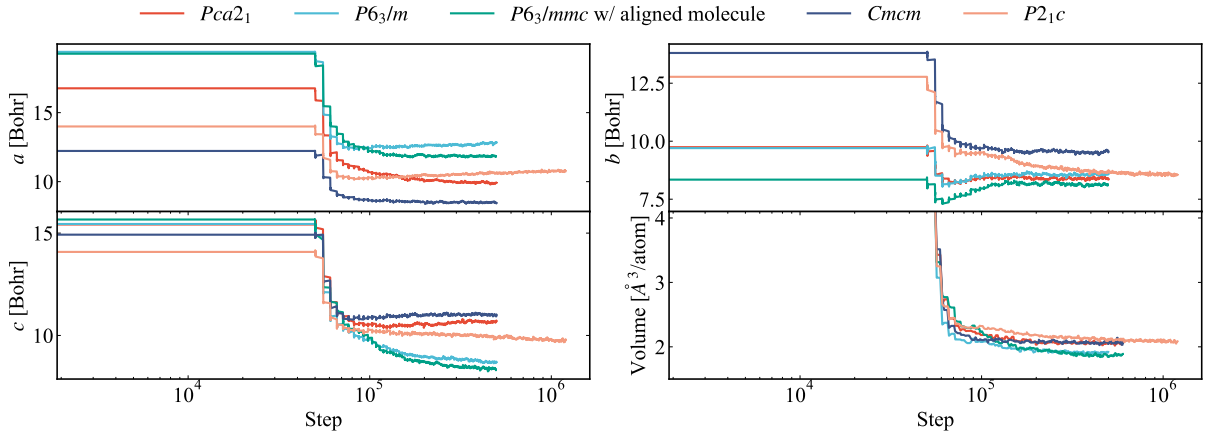


FIG. S3. The evolution of lattice parameters and volume per atoms as a function of training steps. The legend denotes the initial structure.

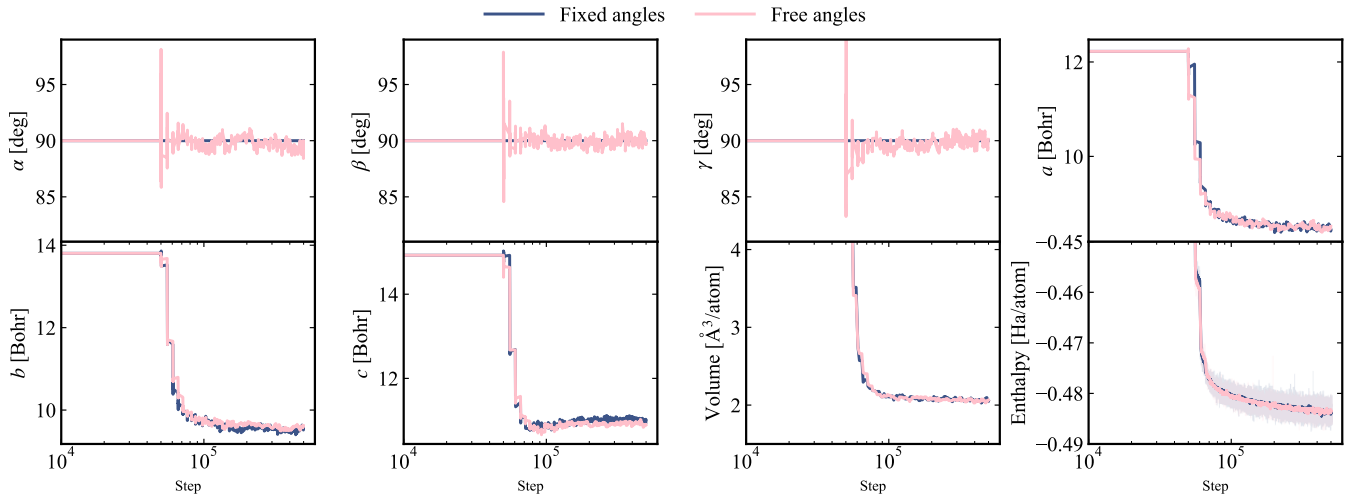


FIG. S4. Comparison between two NPT training runs starting from a $Cmcm$ structure with 64 atoms at 130 GPa: one with cell angles constrained to $\alpha = \beta = \gamma = 90^\circ$ ('Fixed angles') and another with angles freely optimized along with other lattice parameters ('Free angles'). Shaded regions in enthalpy curves represent the original data points, while solid lines show smoothed curves obtained via a moving average with a window size of 1000 steps.

A. Mode of Hydrogen Molecule H_2

A diatomic molecule possesses 6 degrees of freedom (dof):

TABLE IV. The structure identified at 130 GPa for the broken symmetry phase.

Space group	Lattice parameters (Bohr, deg)	Wyckoff position	Fractional coordinates		
			x	y	z
$Cmcm$	$a = 8.48$	8g	0.5992	0.3967	0.2500
	$b = 9.60$	8g	-0.0825	0.2402	0.2500
	$c = 5.47$	8g	0.7642	0.3967	0.2500
	$\alpha = \beta = \gamma = 90.0$	8g	0.4175	0.0867	0.2500

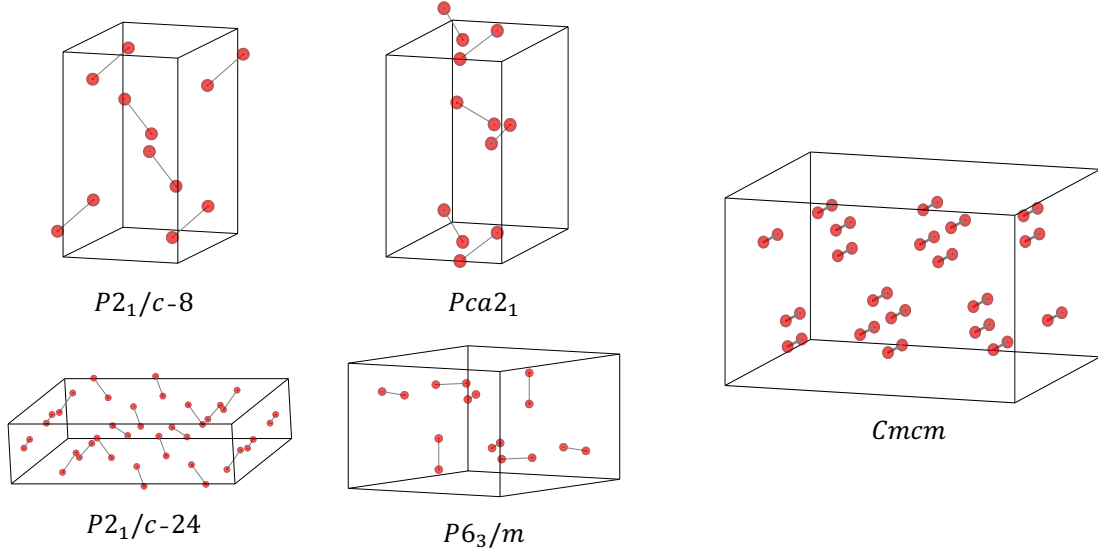


FIG. S5. The structures used in the XRD patterns in Fig. 4. The solid line represents the bonds between the hydrogen atoms, while the box represents the conventional cell for $Cmcm$ and primitive cell for other structures.

1. Translations (3 dof): Basis functions x, y, z , corresponding to $\Pi_u(x, y)$ and $\Sigma_u^+(z)$ representations.
2. Rotations (2 dof): Basis functions R_x, R_y , transforming as $\Pi_g(R_x, R_y)$.
3. Vibration (1 dof): The vibrational mode transforms as Σ_g^+ .

B. Correlation table for $D_{\infty h}$ to site symmetry C_{2v} and C_s

We first restrict the representation in $D_{\infty h}$ into site symmetries C_{2v} and C_s , it can be established from standard correlation relation table.

1. $D_{\infty h} \rightarrow C_{2v}$:
 - $\Sigma_g^+ \rightarrow A_g \rightarrow A_1$
 - $\Pi_g \rightarrow B_{2g} + B_{3g} \rightarrow A_2 + B_1$
 - $\Pi_u \rightarrow B_{2u} + B_{3u} \rightarrow A_1 + B_2$
 - $\Sigma_u^+ \rightarrow B_{1u} \rightarrow B_1$
2. $D_{\infty h} \rightarrow C_s$:
 - $\Sigma_g^+ \rightarrow A_g \rightarrow A'$
 - $\Pi_g \rightarrow B_{2g} + B_{3g} \rightarrow 2A''$
 - $\Pi_u \rightarrow B_{2u} + B_{3u} \rightarrow 2A'$
 - $\Sigma_u^+ \rightarrow B_{1u} \rightarrow A''$

C. Induced Representations in the Factor Group D_{2h}

To determine the representations induced from the subgroups C_{2v} and C_s into the factor group D_{2h} , we employ Frobenius reciprocity. This principle states that the multiplicity of an irreducible representation ρ of a group G in the induced representation of a subgroup H is equal to the multiplicity of the representation of H in the restriction of ρ to H , $\langle \text{Ind}_H^G(\sigma), \rho \rangle_G = \langle \sigma, \text{Res}_H(\rho) \rangle_H$. Consequently, the standard correlation tables from D_{2h} down to C_{2v} and C_s allow us to determine the induced modes.

1. $C_{2v} \rightarrow D_{2h}$:

- (a) $A_1 \rightarrow A_g + B_{2u}$
- (b) $A_2 \rightarrow A_u + B_{2g}$
- (c) $B_1 \rightarrow B_{3g} + B_{1u}$
- (d) $B_2 \rightarrow B_{1g} + B_{3u}$

2. $C_s \rightarrow D_{2h}$:

- (a) $A' \rightarrow A_g + B_{1g} + B_{2u} + B_{3u}$
- (b) $A'' \rightarrow A_u + B_{1u} + B_{2g} + B_{3g}$

D. Raman and IR Active Modes of Solid Hydrogen

Thus, for the vibron:

1. site A(4c): $\Sigma_g^+ \rightarrow A_g \rightarrow A_1 \rightarrow A_g + B_{2u}$
2. site B(4c): $\Sigma_g^+ \rightarrow A_g \rightarrow A_1 \rightarrow A_g + B_{2u}$
3. site C(8g): $\Sigma_g^+ \rightarrow A_g \rightarrow A' \rightarrow A_g + B_{1g} + B_{2u} + B_{3u}$

Thus, the representation of the vibron is

$$\Gamma_{vibron} = 2(A_g + B_{2u}) + (A_g + B_{1g} + B_{2u} + B_{3u}) = 3A_g + 3B_{2u} + B_{1g} + B_{3u} \quad (\text{S8})$$

For the Libron(photon):

1. site A(4c): $\Pi_g \rightarrow B_{2g} + B_{3g} \rightarrow A_2 + B_1 \rightarrow A_u + B_{2g} + B_{3g} + B_{1u}$
2. site B(4c): $\Pi_g \rightarrow B_{2g} + B_{3g} \rightarrow A_2 + B_1 \rightarrow A_u + B_{2g} + B_{3g} + B_{1u}$
3. site C(8g): $\Pi_g \rightarrow B_{2g} + B_{3g} \rightarrow 2A'' \rightarrow 2A_u + 2B_{1u} + 2B_{2g} + 2B_{3g}$

Thus, the representation of the libron is

$$\begin{aligned} \Gamma_{libron} &= 2(A_u + B_{2g} + B_{3g} + B_{1u}) + 2A_u + 2B_{1u} + 2B_{2g} + 2B_{3g} \\ &= 4A_u + 4B_{1u} + 4B_{2g} + 4B_{3g} \end{aligned} \quad (\text{S9})$$

Translational Phonons

1. site A(4c): $\Sigma_u^+ + \Pi_u \rightarrow B_{1u} + B_{2u} + B_{3u} \rightarrow A_1 + B_1 + B_2 \rightarrow A_g + B_{2u} + B_{3g} + B_{1u} + B_{1g} + B_{3u}$
2. site B(4c): $\Sigma_u^+ + \Pi_u \rightarrow B_{1u} + B_{2u} + B_{3u} \rightarrow A_1 + B_1 + B_2 \rightarrow A_g + B_{2u} + B_{3g} + B_{1u} + B_{1g} + B_{3u}$
3. site C(8g): $\Sigma_u^+ + \Pi_u \rightarrow B_{1u} + B_{2u} + B_{3u} \rightarrow 2A' + A'' \rightarrow A_u + B_{1u} + B_{2g} + B_{3g} + 2A_g + 2B_{1g} + 2B_{2u} + 2B_{3u}$

Summing over all sites yields:

$$\begin{aligned} \Gamma_{trans} &= 2A_g + 2B_{2u} + 2B_{3g} + 2B_{1u} + 2B_{1g} + 2B_{3u} \\ &\quad + A_u + B_{1u} + B_{2g} + B_{3g} + 2A_g + 2B_{1g} + 2B_{2u} + 2B_{3u} \\ &= A_u + 4B_{1g} + 4B_{2u} + 3B_{3g} + 4A_g + B_{2g} + 3B_{1u} + 4B_{3u} \end{aligned} \quad (\text{S10})$$

Subtracting the acoustic branches ($B_{1u} + B_{2u} + B_{3u}$):

$$\begin{aligned} \Gamma_{optical} &= \Gamma_{trans} - \Gamma_{acoustic} \\ &= A_u + 4B_{1g} + 3B_{2u} + 3B_{3g} + 4A_g + B_{2g} + 2B_{1u} + 3B_{3u} \end{aligned} \quad (\text{S11})$$

The optical phonon is

$$\Gamma_{optpho} = \Gamma_{optical} + \Gamma_{libron} = 5A_u + 4B_{1g} + 3B_{2u} + 7B_{3g} + 4A_g + 5B_{2g} + 6B_{1u} + 3B_{3u} \quad (\text{S12})$$

Note that A_u modes are silent (inactive in both Raman and IR). In summary, the Raman and IR active modes are:

$$\Gamma_{\text{Raman}}^{\text{vibron}} = 3A_g + B_{1g}, \quad (\text{S13})$$

$$\Gamma_{\text{IR}}^{\text{vibron}} = 3B_{2u} + B_{3u}, \quad (\text{S14})$$

$$\Gamma_{\text{Raman}}^{\text{phonon}} = 4B_{1g} + 7B_{3g} + 4A_g + 5B_{2g}, \quad (\text{S15})$$

$$\Gamma_{\text{IR}}^{\text{phonon}} = 3B_{2u} + 6B_{1u} + 3B_{3u}. \quad (\text{S16})$$

These results identify the Raman- and IR-active vibronic and phononic modes of solid hydrogen in the *Cmcm* phase.